

<https://doi.org/10.1038/s43247-026-03373-7>

Tectonic activity and river mouth proximity drive submarine canyon retreat along Italian coasts

Check for updates

Nicolò Parrino¹, Francesco Caldareri², Pierfrancesco Burrato¹✉, Mimmo Palano^{1,2}, Salvatore Stramondo¹, Valeria Lo Presti², Mauro Agate², Maurizio Gasparo Morticelli^{1,2} & Attilio Sulli^{1,2}

Active tectonics and coastal deformation predispose continental margins to submarine gravitational instability and canyon head retreat. Here we investigate the drivers of this susceptibility along the Italian coasts. We analyze a dataset of over 2700 canyon heads using a multi-parametric susceptibility model that integrates bathymetry, instrumental seismicity, uplift rates, and crustal deformation fields derived from satellite geodesy. Results indicate that proximity to river mouths and regional seismicity are primary drivers of retreat susceptibility, suggesting that such susceptibility characterizes canyon dynamics at least since the establishment of the current tectonic regime. By integrating these results with demographic exposure data, we identify priority areas for mitigating natural disasters such as landslide-generated tsunamis and coastal erosion in highly populated regions.

Submarine Canyons (hereafter, SCs) represent some of the most massive and dynamic morphological feature in marine landscapes, which represent a preferential sediment escape way to the abyssal plain or intraslope basin^{1–3}. These landforms could incise continental margins from continental platform/slope to abyssal plains, or can be confined into the continental slope only^{4–8}.

The present study focuses on SCs that cut the shelf-break landward. Their dynamic nature makes them critical components in Earth's sedimentary systems, affecting oceanographic processes, sediment routing, and marine ecosystem development and distribution^{9,10}. Given the size of these landforms, the SCs' growth therefore constitutes one of the principal mechanisms of offshore landscape evolution. As with many other Quaternary geological processes, the study of landscape evolution allows to disentangle the tectonic and climatic forces driving the development of SC, thereby enhancing our understanding of their associated geohazards^{11–18}.

SCs can evolve through two mechanisms depending on the dominant erosional processes. Top-down canyons develop through turbidity currents and sediment-gravity flows originating from the continental shelf or through underwater landslides starting from the SCs head. Conversely, bottom-up processes involve retrogressive erosion at canyon heads through mass-wasting events that propagate upslope^{6,19,20}. This manuscript focuses on SCs whose evolution is dominated by headward retrogressive processes and on the potential geohazards that such mechanisms may drive in coastal areas. While retrogressive SCs occur globally, their proximity to coastal areas and associated hazard potential vary depending on continental margin architecture. In the Atlantic Ocean, for example, canyons typically indent the shelf but remain several kilometers offshore due to wider continental

shelves²¹. In contrast, the Mediterranean Sea presents distinctive characteristics, with tectonically controlled narrow shelves and steep margins facilitate the development of shelf-incising canyons with heads located near or directly adjacent to the coastline²². This geological configuration, enhanced by high seismicity, correlated with high tectonic uplift rates, and sediment supply from steep coastal catchments, makes Mediterranean SCs particularly relevant for coastal geohazard assessment, as retrogressive processes can directly threaten nearshore infrastructure and population centers^{3,19,23}. Canyon heads undergoing retrogressive retreat represent critical zones where erosion directly impacts the shelf and nearshore environments, potentially involving massive submarine landslides that can drive hazards to modern societies, such as tsunamis and coastal erosion^{7,24,25}.

These geohazards are especially related to regions where SCs intersect narrow continental platform shelf break adjacent to densely populated coastal communities, whose retreat may affect the shoreline, which can be monitored using recently developed remote sensing techniques employing multispectral imagery to track its position^{13,18,26}. While individual case studies have explored the relationship between retrogressive erosion of canyon heads and related hazards^{4,22,27–32}, a large-scale comprehensive analysis incorporating a statistically noteworthy number of cases is so far lacking. Thus, local drivers of submarine canyon retreat have been frequently explored, and the implications of the results have subsequently been generalized conceptually. However, regional case studies that would allow for the investigation of the drivers of canyon retreat at a lower level of abstraction, and therefore more robustly, are still limited and often analyze the problem at a scale too large to robustly isolate the forces for canyon retreat^{2,33,34}. Considering the above, a fundamental scientific question

¹Istituto Nazionale di Geofisica e Vulcanologia, Rome, Italy. ²Università degli Studi di Palermo, Palermo, Italy. ✉e-mail: pierfrancesco.burrato@ingv.it

remains unresolved: what are the primary drivers controlling canyon head retreat? While recent global studies have highlighted the role of river discharge and tectonic activity in maintaining canyon connection, understanding this process requires assessing susceptibility, the inherent spatial predisposition of a site to undergo retrogressive failure, independent of temporal frequency, which represents a fundamental component of hazard evaluation²¹. Equally important is the challenge of quantifying the associated hazard potential to inform risk management strategies for vulnerable coastal communities. The significance of these geohazards has become increasingly critical as global coastal population density continues to rise, with over 600 million people currently residing in low-elevation coastal zones less than 10 m above sea level especially in tourist areas that meaningfully increase their population density in specific period of the year^{35–38}. The Italian continental margins (central Mediterranean Sea, Fig. 1) provide an ideal natural laboratory for addressing these research questions, offering different tectonic settings, abundant SCs, and extensive high-resolution datasets on bathymetry (e.g., the MaGIC project dataset⁴), vertical tectonic differential ground movements (considering both the long-term deformation depicted from morphotectonic related paleo-geodetic indicator and also instrumental dataset, such as satellite geodesy data), seismicity, and coastal demographics that enable integrated analysis of multiple contributing factors.

By analyzing over 2700 shelf-indenting canyon heads incising the Italian continental margins and correlating them with tectonic and morphological variables (described in the section 3.1), we aim to enhance understanding of the primary Quaternary geological processes driving canyon head retreat and their associated hazards. Our methodology integrates multiple independent variables, including high-resolution bathymetry, crustal velocity and strain-rate fields, earthquake density 2D distribution, and coastal proximity metrics, to develop a robust statistical framework that quantifies canyon retreat susceptibility while elucidating the relative contribution of each geological, geophysical and morphological factor.

Seismotectonic and Morphologic setting

The Italian continental margin encompasses several sub-basins of the central Mediterranean Sea. These sub-basins display diverse bathymetric and structural settings, underlain by old Mesozoic Tethyan and Neogene oceanic crusts as well as thick continental lithosphere. Their present-day geodynamic framework results from the protracted convergence and slow collision between the African and Eurasian plates^{39–41}, which has driven the formation of the Apennine-Maghrebian orogenic system and the opening of the Tyrrhenian back-arc basin through eastward roll-back of the Adriatic-Ionian slab^{42–44} (Fig. 1).

Within this geodynamic context, the study area can be subdivided into five distinct seismotectonic domains characterized by contrasting fault kinematics, seismicity patterns, and deformation rates^{45–47}: (1) back-arc extensional basins, including the Tyrrhenian Sea margins, formed by post-Miocene rifting, thin oceanic or transitional crust, and widespread active volcanism^{48,49}; (2) extensional belts, comprising zones of active normal faulting along the Tyrrhenian margins and inner Apennines, where seismicity is dominated by high-angle normal faults accommodating ongoing extension perpendicular to the chain⁵⁰; (3) active orogenic belts, including the Calabrian Arc and portions of the external Apennines and Siculo-Maghrebian thrust system, where reverse and strike-slip faulting accommodates ongoing convergence and lateral tectonics^{16,51–54}; (4) foreland basins, encompassing the Adriatic and Ionian and the Sicily Channel deformed margins, characterized by flexural subsidence, thrust-related folding, the moderate compressional seismicity^{55–57}; and (5) stabilized old orogenic belts, representing ancient, seismically quiescent portions of the thrust belt where deformation has ceased or diminished⁵⁸.

A main tectonic feature is represented by the Calabrian subduction zone, where remnant Ionian oceanic lithosphere subducts beneath the Calabrian Arc at a steep angle ($\sim 70^\circ$), generating the deepest seismicity in the Mediterranean region (down to 500 km)^{59,60}. This narrow subduction

system creates vertical differential movements, with rapid tectonic uplift rates (up to 1–2 mm/yr) along the Ionian coast of Calabria^{61,62}, contrasting with slow uplift or subsidence in the adjacent foreland, producing steep submarine slopes and remarkable shaking frequency⁶³. The spatial distribution of seismicity (Fig. 1d) reflects this complex geodynamic partitioning, with shallow crustal earthquakes concentrated along the actively deforming extensional and compressional belts, while intermediate-depth and deep compressional seismicity characterizes the Calabrian subduction zone⁶⁴. Active volcanism (Fig. 1d) is predominantly confined to the Tyrrhenian back-arc domain and the Calabrian Arc, including the Aeolian Islands, Mount Etna, and submarine volcanic complexes^{65,66} (many of which show evidence of Holocene activity⁶⁷), further distinguishing these actively deforming settings from the almost stable foreland domains.

Submarine Canyons (SCs)

SCs are steep-walled valleys that typically exhibit low overall sinuosity in both active and passive margin settings, occur on slopes and evolve under gravitational processes^{1,3,34,68–71}. They comprise distinct morphologies: the head (which may incise the shelf break or remain confined to the slope), the walls, the main channel, and tributaries (also called gullies)^{72–75}. Based on their morphology and relationship with the continental shelf, SCs can be categorized as follows: Type 1, which incise the shelf and are connected to a river system; Type 2, which also incise the shelf but have no river connection; and Type 3, known as ‘blind’ canyons, which are restricted entirely to the continental slope^{3,23,68,69}. A comprehensive global mapping study identified 9477 SCs worldwide, covering approximately 4.4 million km² (1.2% of the ocean floor) and comprising an average of 11.2% of the global continental slope area. Shelf-incising SCs (which cut across the shelf break) are substantially larger than their blind counterparts, with average sizes of 777 km² and mean lengths of 54.8 km, compared to 375 km² and 37.3 km for blind SCs (confined to the slope)⁷⁶. In the present study, we extracted the highest point for each mapped detachment niche as a unique identifier. This approach enabled the creation of a nationwide point-based inventory of SCs in Italy. Each point record in this inventory is referred to as Punto Identificativo del Canyon Sottomarino (PICS, Identification Point of the Submarine Canyon, see Fig. 2).

As mentioned above, the evolution of SCs is driven by a complex interplay between large-scale controlling factors, such as tectonic activity and climate-driven cycles. These factors, in turn, govern submarine landslides, turbidity currents, and dense shelf water cascading, which are responsible for canyon incision and maintenance^{2,23,75,77}. Retrogressive erosion of canyon heads represents a critical evolutionary process since it can affect anthropogenic coastal assets. Despite this, the relation between the SCs and their regional tectonic setting in shaping canyon geomorphology and influencing sediment transport dynamics is not fully explored, even if global-scale studies demonstrated that the relation between SCs morphology and, especially, concavity is influenced by tectonic setting^{3,78,79} and that the slope failure processes could be more important in passive-margin⁸⁰.

These seafloor features serve crucial functions in Earth’s sedimentary systems, facilitating sediment transport from continental shelves to deep marine basins mainly through density flows^{80–84}. They influence oceanographic processes, benthic ecosystem distribution, marine pollution pathways and carbon sequestration pathways^{80,84–87}. Submarine landslides originating from shelf-incising canyon heads pose geohazards to coastal regions through multiple mechanisms: direct tsunami generation from mass failure, progressive ground destabilization and nearshore erosion due to retrogressive undermining of the coastal foundation, and damage to seafloor infrastructure. However, assessing these hazards is challenging due to the nearshore data gap caused by limitations in ship-based bathymetric surveys in shallow waters (the white ribbon), which restricts our ability to fully characterize canyon head morphology and dynamics in the most vulnerable coastal zones^{28,88,89}. Climate change may affect sediment circulation frequency and intensity within these systems, potentially altering deep-sea ecosystems and carbon storage mechanisms on continental margins².

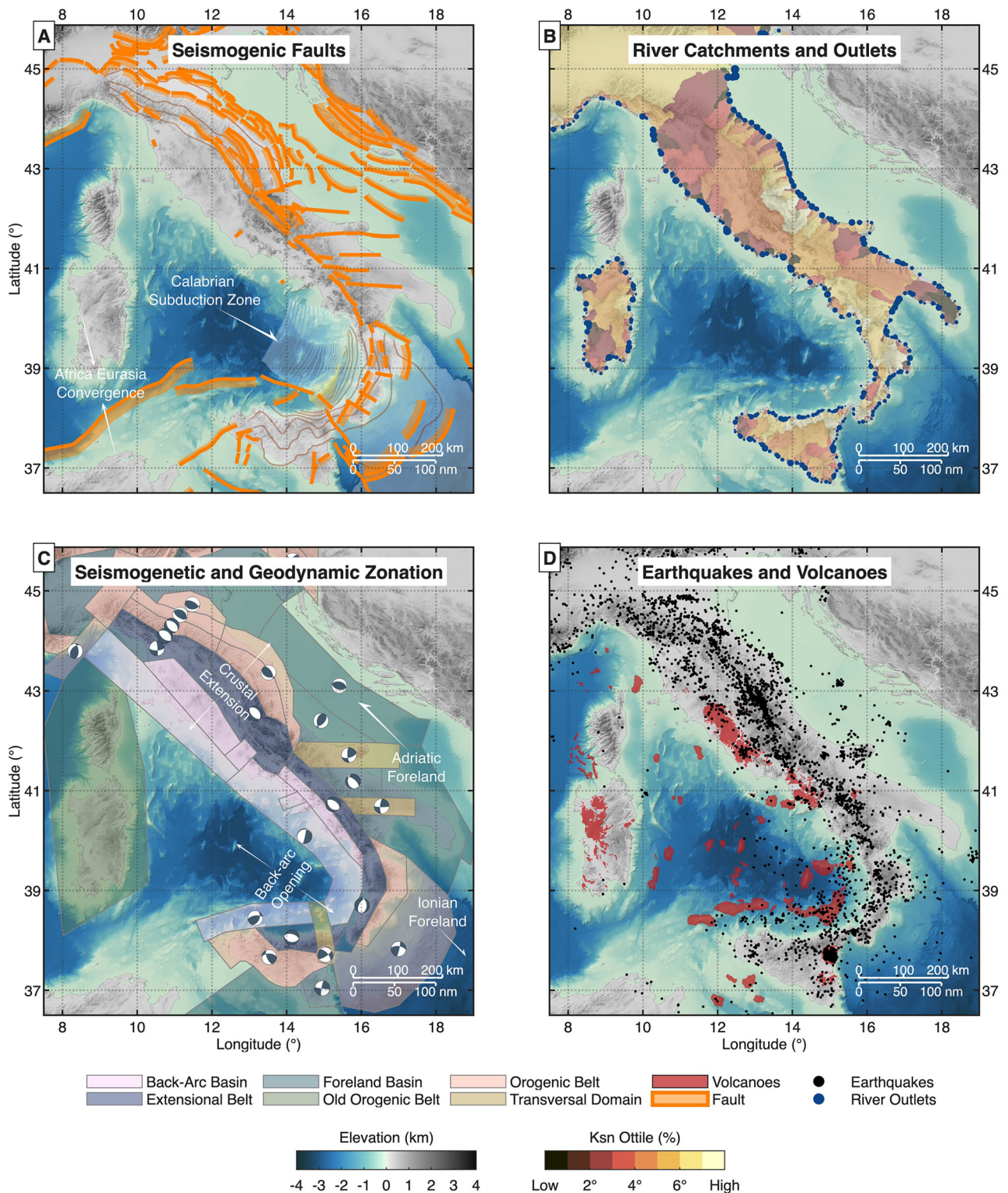


Fig. 1 | Seismotectonic and morphologic setting of the Italian continental margin. **A** Potential sources of large earthquakes, including crustal active faults (orange ribbons) and subduction interfaces (shown with gray contours) from the DISS database¹⁴¹. **B** River catchments color-coded according to their average Ksn and river mouths (blue dots with variable size according to the flow accumulation of the

related drainage basin). **C** Area-source seismogenic model, geodynamic zonation and expected focal mechanisms for each area^{45,46}. **D** Quaternary volcanoes and historical and instrumental seismicity with $M_W \geq 4.0$ from the INGV CPTI catalog¹⁶⁴.

Results

All the canyon heads mapped within the submarine canyon headwalls yielded a total of 2765 mapped PICS along nearly the entire Italian coastline, with d_{pc} values ranging from a few meters to approximately

69 km (please refer to Table 1 for the full acronym list used in this manuscript).

This comprehensive database of values served as the set of dependent variables for subsequent exploration of relationships between canyon retreat

Fig. 2 | 3D topo-bathymetric view of the Gulf of Palermo (Italy). The map shows Submarine Canyon (SCs) headwalls along the continental slope. The pink dashed line marks the shelf edge, red lines indicate canyon heads, and black dots represent the Punto Identificativo del Canyon Sottomarino (PICS, Identification Point of the Submarine Canyon). The vertical scale is exaggerated ten times. Topography is from Regione Siciliana LiDAR dataset and bathymetry from MaGIC multibeam data^{122,165}. The black polygon in the inset shows the location of the Area of Interest (AOI) on the geoid (topographic data from ETOPO¹⁶⁶).

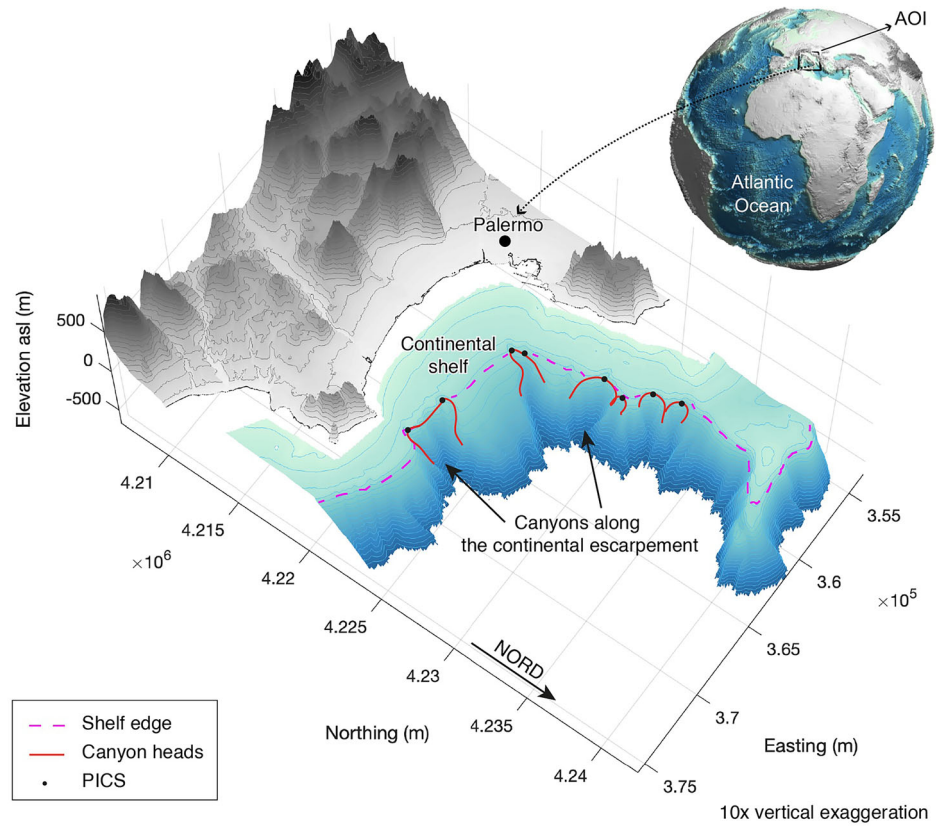


Table 1 | Tectonic and morphologic independent variables used in this study

#	Variable	Variable meaning
1	d_{Pr}	The minimum distance between each PICS and the nearest river mouth
2	d_{Pc}/d_{Pr}	The degree of alignment between the PICS and nearest river mouths
3	$r_{FlowAcc}$	Flow Accumulation at the PICS nearest river mouth
4	r_{Ksn}	Stream network averaged normalized steepness index at the PICS closest river mouth
5	RM	A relief metric computed as the weighted average between relief and topographic variance, with equal weight assigned to both terms
6	s	The topographic slope value computed in the PICS location
7	$GNSS_v$	GNSS vertical velocity field
8	$GNSS_h$	GNSS horizontal velocity field
9	$GNSS_{2inv}$	The 2nd invariance of horizontal strain rate values
10	$EGMS_{avg}$	InSAR coastal vertical deformation
11	F_{06}	Uplift rate computed from the literature of MIS 5.5 paleoshorelines elevation
12	$CPTI_{15}$	Instrumental earthquake seismic moment distribution
13	$DISS_{snt}$	Synthetic earthquake seismic moment distribution

The first column includes the progressive numbering also reported in the text, the second column reports the variable acronyms, while the third column reports a brief explanation of the variable meaning.

susceptibility and various regressors. Regarding the independent variable transformation analyses, the results are summarized in the Supplementary Information (Supplementary Table 1).

Logarithmic transformation emerged as the best-fit model for both raw and standardized data, optimal for six and four variables, respectively,

followed by the square root transformation (three variables for raw data) and the quadratic transformation (three variables for standardized data). The highest coefficient of determination (R^2) value (0.48) was observed for the distance between each PICS and the nearest river mouth with logarithmic transformation applied to raw data, while the lowest (0.0005) was found for the second invariant of strain rate. For standardized variables, the second invariant of the GNSS horizontal velocity field showed the highest R^2 (0.21) with quadratic transformation.

The Akaike's Information Criterion (AIC) values showed consistent patterns with R^2 improvements, with the lowest values for the distance to the nearest river mouth (6023.60 for raw data, 6430.26 for standardized data), indicating the best overall model fit among all variables. Standardization improved model performance for several variables, most notably for the second invariant of strain rate (improvement of 46.13%) and topographic variance (improvement of 39.68%). Conversely, other variables, such as slope and distance to the nearest canyon axis, performed better in their raw form, showing negative improvements of -46.68% and -46.41% respectively (see Supplementary Table 1 for more information).

The Multiple Linear Regression Models

The Variance Inflation Factors (VIF) analysis demonstrated that multicollinearity is not a concern for the independent variables in this study. All VIF values remained well below the critical threshold of 5, with the highest values observed for $CPTI_{15}$ (2.45), $DISS_{snt}$ (2.36), and F_{06} (2.34), while the lowest was found for $GNSS_v$ (1.10). This indicates that the independent variables maintain sufficient distinctiveness in the model (Supplementary Table 1). The correlation analysis identified six relationships with absolute correlation coefficients exceeding 0.5, with the strongest being the positive correlation between $CPTI_{15}$ and $DISS_{snt}$ ($r = 0.649$), followed by F_{06} and $CPTI_{15}$ ($r = 0.606$). Notable negative correlations were observed between F_{06} and D_{Pr} ($r = -0.584$) and between D_{Pr} and $CPTI_{15}$ ($r = -0.561$).

As shown in Fig. 3a–d and Supplementary Table 2, both regression models achieved exceptionally high explanatory power, with R^2 values exceeding 99%. The Huber model demonstrated slightly superior variance

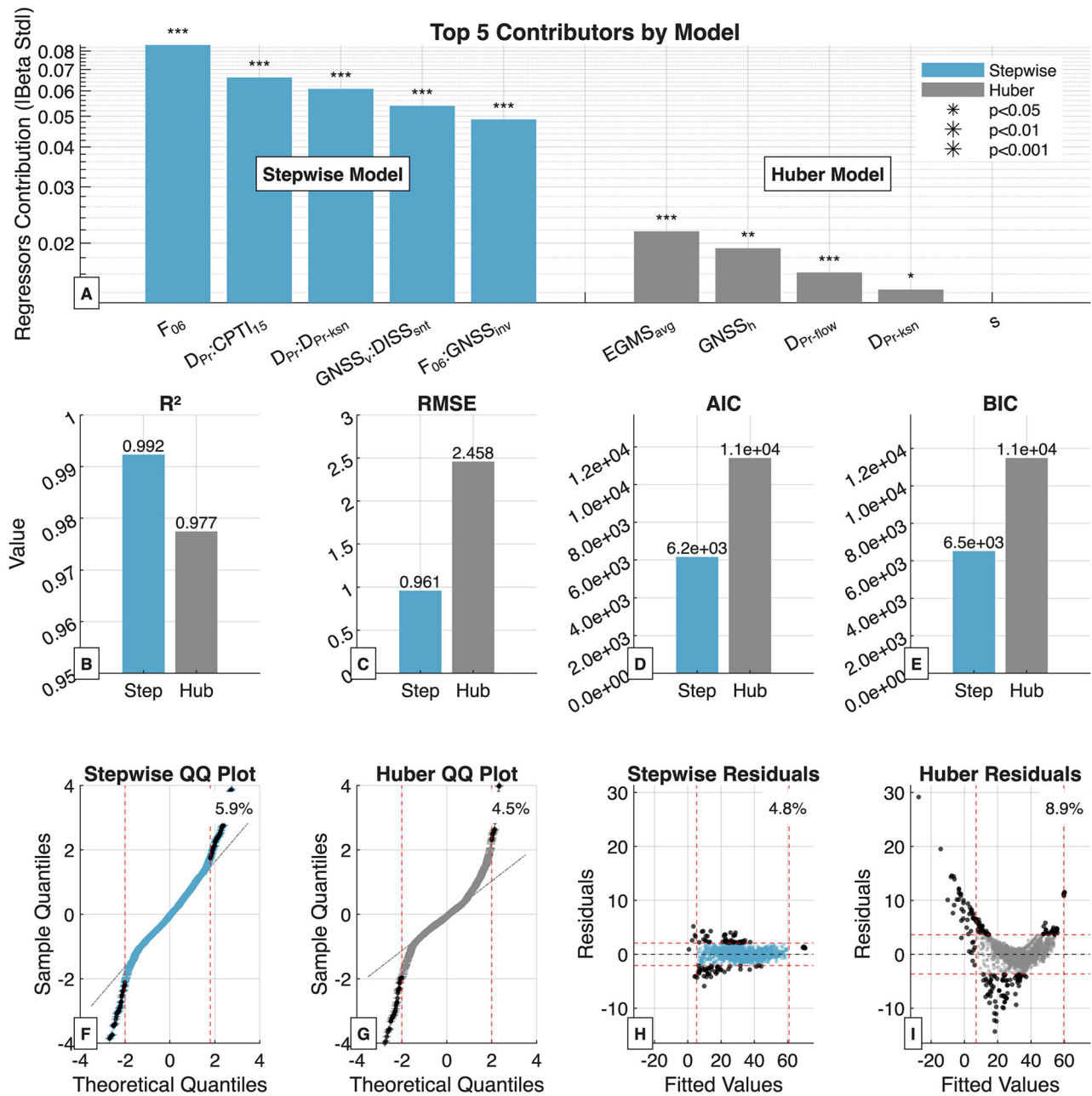


Fig. 3 | Statistical validation and model comparison for the Stepwise and Huber regression models. A–D Performance metrics comparison between models: A coefficient of determination, B Root Mean Square Error, C Akaike Information Criterion and D Bayesian Information Criterion. E, F Quantile-Quantile plots for the Stepwise and Huber models, with outliers in black dots and ± 2 standard deviation

thresholds as red dashed lines. G, H Residuals versus fitted values plots with outliers (black dots) and Interquartile Range boundaries (red dashed lines). Percentages show outlier proportions. I Top five regressors contribution for both models, with significance levels indicated by asterisks.

explanation ($R^2 = 0.997$, adjusted $R^2 = 0.997$) compared to the Stepwise model ($R^2 = 0.992$, adjusted $R^2 = 0.992$). However, the models exhibited contrasting strengths in different performance metrics. The Stepwise model showed superior predictive accuracy with substantially lower error metrics (Root Mean Square Error (RMSE) = 0.961, Mean Absolute Error (MAE) = 1.08) compared to the Huber model (RMSE = 1.65, MAE = 1.77). The Stepwise model also demonstrated better parsimony, with markedly lower information criteria values (AIC = 6160, Bayesian Information Criterion (BIC) = 6520) compared to the Huber model (AIC = 12800, BIC = 12,900), reflecting its more efficient model structure. Both models showed evidence of heteroscedasticity, with White’s test yielding χ^2 values of 42,000 (Stepwise) and 259,000 (Huber), and Breusch-Pagan test statistics of 632 (Stepwise) and 1280 (Huber), all with $p < 0.001$.

The outlier analysis revealed complete concordance between the two models. Quantile-quantile (QQ) analysis identified 148 anomalous observations in each model, while residual-based analysis detected 138 outliers in both models. This perfect consistency in outlier identification across both analytical approaches and regression methods indicates that approximately 5% of the dataset ($n = 2765$ PICS) consists of observations with unusual retreat patterns (Fig. 3e–h and Supplementary Tables 2).

The Stepwise regression model incorporated 62 coefficients: one intercept term, 13 main effects, and 48 two-way interaction terms. White’s heteroscedasticity-robust estimation identified several dominant predictors (Supplementary Table 3 and Supplementary Equation 1). Among the main effects, the distance-related parameters showed the most substantial influence: D_{Pc}/D_{Pr} exhibited the strongest positive coefficient (29.457,

$p < 0.001$), followed by D_{Pr} (9.180, $p < 0.001$), while F_{06} showed a strong negative effect (-2.956 , $p < 0.001$). The interaction terms revealed complex relationships, with $D_{Pr} : D_{Pc}/D_{Pr}$ showing the strongest positive interaction (7.541, $p < 0.001$), and $F_{06} : RM$ displaying the strongest negative interaction (-6.139 , $p < 0.001$). Other notable interactions included $D_{Pr} : r_{Ksn}$ (-0.602 , $p < 0.001$) and $F_{06} : D_{Pr}$ (-1.750 , $p < 0.001$), indicating that the effects of distance parameters are substantially modulated by topographic and relief characteristics.

The analysis revealed substantial differences between the original and White's standard errors across multiple parameters. In the Stepwise model, the most pronounced variation was observed for $D_{Pr} : D_{Pc}/D_{Pr}$ (114% difference), followed by $D_{Pr} : r_{Ksn}$ (105%) and

$D_{Pc}/D_{Pr} : CPTI_{15}$ (87%). Four interaction terms exhibited changes in statistical significance when applying White's robust standard errors: $F_{06} : DISS_{snt}$, $GNSS_{inv} : D_{Pr}$, $D_{Pc}/D_{Pr} : RM$, and $D_{Pc}/D_{Pr} : CPTI_{15}$. The Stepwise model, which includes 62 coefficients (1 intercept, 13 main effects, and 48 interaction terms), is formally represented by the equation shown in Supplementary Equation 1.

For the Huber model (Supplementary Table 4), the robust estimation analysis examined 14 main effect parameters without interaction terms. The distance-related parameters showed the strongest effects: D_{Pc}/D_{Pr} exhibited the highest positive coefficient (28.521, $p < 0.001$), followed by D_{Pr} (9.190, $p < 0.001$). Among the negative coefficients, $EGMS_{avg}$ showed the strongest effect (-0.894 , $p < 0.001$), followed by RM (-1.046 , $p = 0.027$) and $GNSS_h$ (-0.196 , $p = 0.001$). The geodetic variables maintained their significance, with $GNSS_{inv}$ showing a substantial positive coefficient (0.965, $p < 0.001$). The Huber model exhibited even larger variations in standard errors than the Stepwise model, with D_{Pr} showing the largest difference at 292%, followed by $GNSS_v$ (91%) and s (86%). Only two variables experienced changes in statistical significance under White's robust estimation: s (p -value shifted from 0.0003 to 0.052) and $GNSS_v$ (p -value shifted from 0.033 to 0.262). The Huber model is formally represented by the Supplementary Equation 2.

Regressor Contribution to Susceptibility

The analysis of robust White coefficients' contributions to submarine canyon head retreat susceptibility in the Stepwise model reveals an exceptionally wide range of influences, spanning 20 orders of magnitude (from 10^{18} to 10^{-2} units, see Fig. 3i, Fig. 4a and Supplementary Table 5). The model demonstrates a clear hierarchy dominated by interaction effects involving seismic density parameters. The five highest contributors, all exceeding 10^{17} units, are exclusively interaction terms where $DISS_{snt}$ interacts with other variables. These are $r_{FlowAcc} : DISS_{snt}$ (6.37×10^{18} , $p = 0.005$), $r_{Ksn} : DISS_{snt}$ (2.54×10^{18} , $p < 0.001$), $GNSS_{inv} : DISS_{snt}$ (1.70×10^{18} , $p < 0.001$), $GNSS_h : DISS_{snt}$ (1.28×10^{18} , $p < 0.001$), and $GNSS_v : DISS_{snt}$ (3.36×10^{17} , $p < 0.001$). Beyond seismic interactions, the model identifies important contributions from earthquake catalog parameters, with $D_{Pr} : CPTI_{15}$ (1.28×10^{12} , $p < 0.001$) and several other $CPTI_{15}$ interaction terms ranging from 10^9 to 10^8 units. Individual variables show markedly lower contributions than interaction terms, with $D_{Pr} : r_{Ksn}$ (2.39×10^5 , $p < 0.001$) and D_{Pr} (1.10×10^5 , $p < 0.001$) being the only non-interaction terms approaching 10^5 units, suggesting that the interplay between variables is substantially more important than their individual effects in determining susceptibility.

The Huber model reveals a contrasting pattern with a simpler structure spanning 17 orders of magnitude (from 10^{16} to 10^{-1} units, Fig. 3i and Supplementary Table 5). This model contains only main effects without interaction terms. The contribution hierarchy is dramatically dominated by a single variable: $DISS_{snt}$ shows an exceptionally high contribution of 8.58×10^{16} ($p < 0.001$), approximately nine orders of magnitude larger than the second-ranked variable. This is followed by $CPTI_{15}$ (2.10×10^7 , $p = 0.350$), and D_{Pr} (1.10×10^5 , $p < 0.001$). The remaining variables show contributions below 10^2 units, with $r_{FlowAcc}$ (82.6, $p < 0.001$) and D_{Pc}/D_{Pr} (17.7, $p < 0.001$) completing the top five contributors.

Comparison of the two models reveals fundamentally different architectures for explaining canyon head retreat susceptibility (Fig. 4b). The

Stepwise model distributes explanatory power across numerous interaction terms, with seismic density ($DISS_{snt}$) acting as a key moderator in the top five interactions, contributing cumulatively through its interactions with hydrological ($r_{FlowAcc}$, r_{Ksn}) and geodetic ($GNSS$) parameters. In contrast, the Huber model concentrates explanatory power in $DISS_{snt}$ as a dominant individual predictor (8.58×10^{16}), with earthquake catalog density ($CPTI_{15}$) and distance to river mouth (D_{Pr}) providing secondary contributions that are nine and 11 orders of magnitude smaller, respectively. The D_{Pr} parameter maintains relevance across both models, appearing as an individual variable in both approaches (1.10×10^5 in each), though in the Stepwise model it gains additional importance through its interactions with seismic parameters ($D_{Pr} : CPTI_{15} = 1.28 \times 10^{12}$, $p < 0.001$). This contrast suggests that while seismic forcing is critical in both models, the Stepwise approach captures complex nonlinear relationships through interactions, whereas the Huber method prioritizes a simpler additive structure dominated by fault-related seismicity.

Geodynamic Control on Susceptibility Patterns

The PICS aggregation within the seismogenic zones revealed pronounced variations in submarine canyon head retreat susceptibility across different geodynamic settings (Figs. 1C and 4C, D, Supplementary Table 6). Median susceptibility values ranged from 2 (reverse-faulting old orogenic belt) to 10 (reverse-faulting back-arc basin, normal-faulting extensional belt, and reverse-faulting active orogenic belt). The consistency metric revealed marked differences in spatial homogeneity of susceptibility within zones. Eight zones (36% of total) exhibited perfect consistency (value = 1.0, Interquartile Range method (IQR) = 0), indicating spatially uniform susceptibility entirely controlled by regional geodynamic forcing, such as high-susceptibility back-arc basin and orogenic belt zones. Conversely, foreland basin settings displayed the lowest consistency values, reflecting strong modulation of susceptibility by local factors beyond regional tectonics, as expected in slower deforming areas. Aggregation by fault kinematic regime (see Supplementary Table 6) revealed systematic patterns: normal-faulting extensional belts exhibited high median susceptibility (9) with moderate spatial variability (IQR = 4); reverse-faulting active orogenic belts ($n = 82$ PICS) showed the highest median susceptibility (10) with high consistency (median consistency = 0.79); strike-slip orogenic belts ($n = 495$ PICS) displayed intermediate susceptibility (median = 7) and moderate consistency (0.58). Notably, the large reverse-faulting old orogenic belt dataset ($n = 707$ PICS) presented anomalously low susceptibility (median = 2) despite compressional tectonics. The spatial distribution of high-consistency zones (Fig. 4D) identified geodynamic settings where canyon retreat susceptibility is both elevated and spatially predictable, including the Calabrian subduction zone and portions of the northern Tyrrhenian extensional belt.

Priority Assessment Results: Critical Hotspots Identification

The area-wide exposure metric, quantifying cumulative demographic pressure within 10 km buffers around each PICS, was computed for 1,754 canyon heads (63.4% of the total dataset, see Fig. 5). The calculation incorporated an average of 7.4 ± 4.4 municipalities per PICS, indicating substantial variability in the density of coastal settlements surrounding different canyon systems. The resulting metric values ranged from 0.0037 to 0.7071. When classified into ten quantile-based classes, the distribution was approximately uniform across all classes, with each containing between 9.18% (class 10, highest exposure) and 10.60% (class 7) of the dataset. The composite priority score ranged from 6.7 to 86.7 across the analyzed PICS. The top 97 highest-priority canyon heads (3.51% of the dataset) exhibited composite scores 80.0, with all sites displaying maximum proximity exposure (class 10) combined with variable but elevated values in the other two components (mean susceptibility class 6.5, mean area-wide exposure class 8.3), indicating that the highest-priority sites are characterized by the convergence of extreme local demographic pressure with elevated geological susceptibility and regional exposure. The adaptive threshold analysis for multi-criteria hotspot identification revealed that at threshold 6, 113 PICS (4.09%) satisfied all three criteria simultaneously. Increasing the threshold to

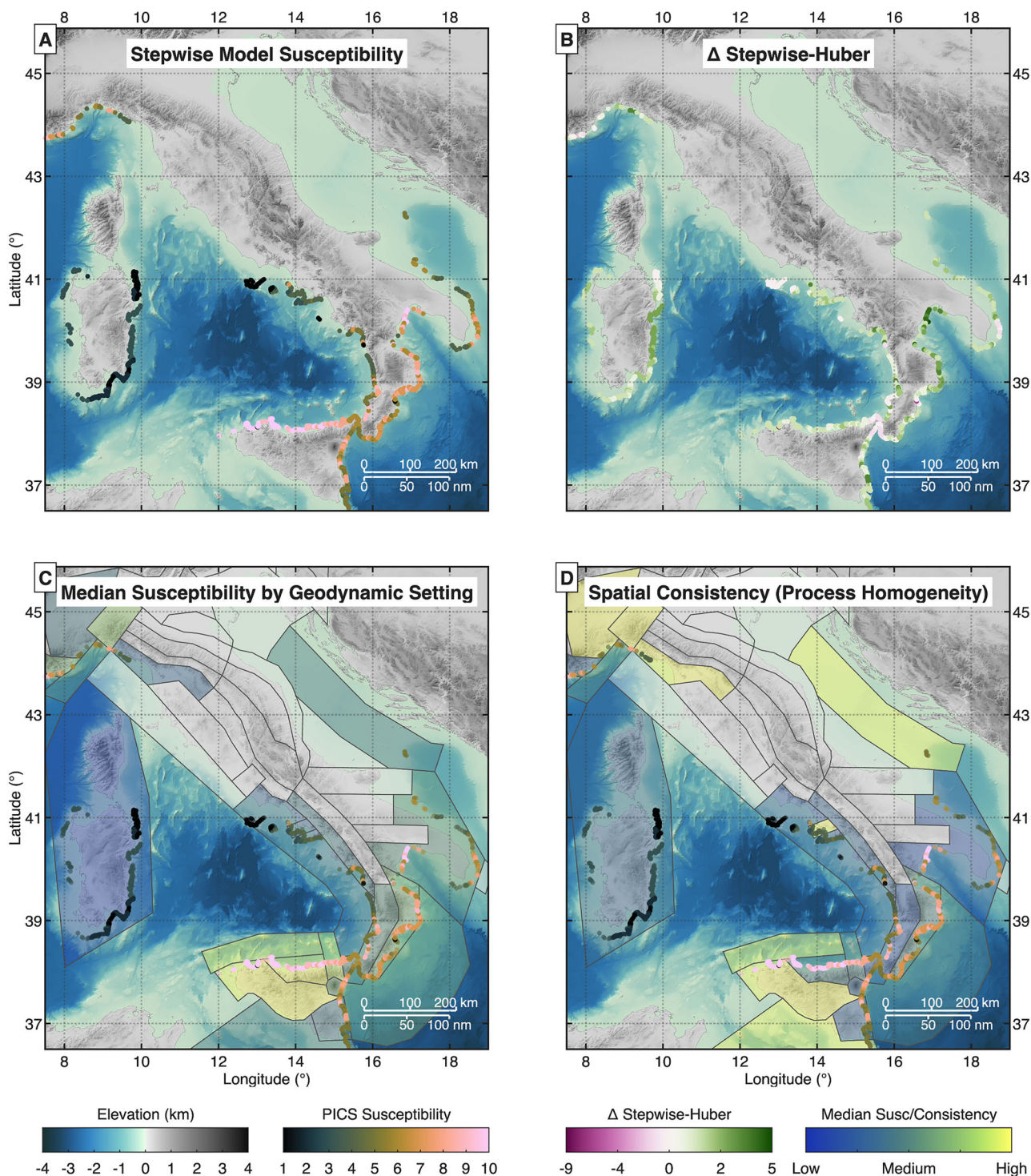


Fig. 4 | Spatial distribution and geodynamic control of submarine canyon susceptibility. **A** Quantile classification of PICS based on the Stepwise susceptibility model (for interpretation of the colors of the dots representing the PICS refer to the second colourbar from the left for classification range 1–10). **B** Spatial comparison between Stepwise and Huber susceptibility models, displaying classification differences (Δ values shown in the third colourbar, range -9 to $+5$). Positive values indicate higher susceptibility in the Stepwise model, while negative values suggest the Huber model assigns greater susceptibility. **C** Median susceptibility aggregated by geodynamic setting (ZS16 seismogenic zones). Polygon colors represent the median PICS susceptibility within each zone, enabling direct comparison with **(D)** through a

unified color scale (rightmost colourbar, Low–Medium–High). **D** Spatial consistency (process homogeneity) within geodynamic zones. Polygon colors indicate the consistency weight (inverse of interquartile range), with higher values (lighter colors) representing homogeneous landslide processes dominated by tectonic forcing, and lower values (darker colors) indicating heterogeneous, multi-factor-controlled environments requiring site-specific analysis. The unified color scale facilitates direct visual comparison between **(C)** and **(D)**, where matching colors across both panels identify process-dominated zones, while contrasting colors reveal complex, spatially variable susceptibility patterns. The leftmost colourbar indicates bathymetric elevation (km).

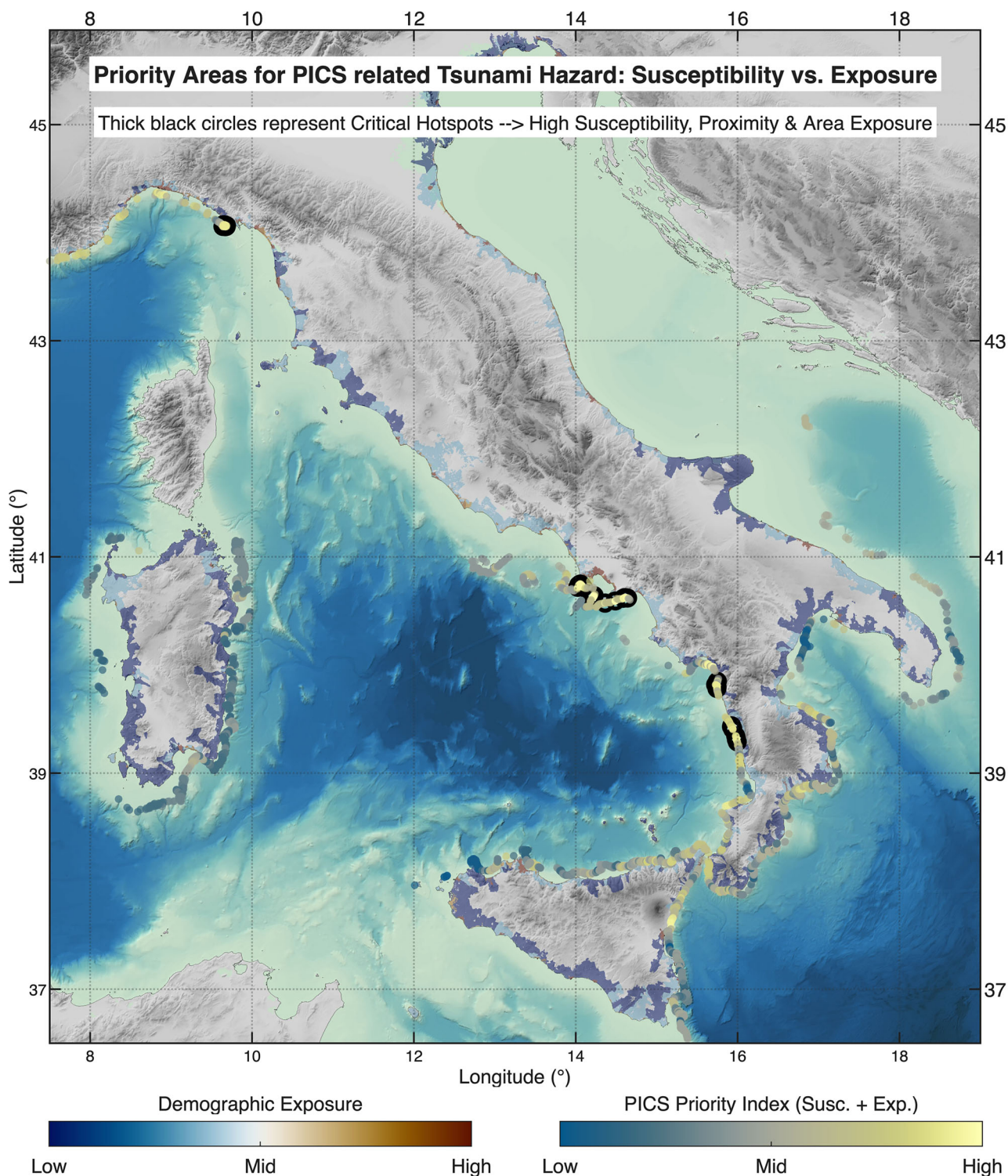


Fig. 5 | Demographic exposure along the Italian coastline. The exposure was computed within 10 km-radius circular buffer areas around the canyon heads considering the Priority Index of the PICS. The map shows the location of the 74 highest-priority sites. (Critical Hotspots) highlighted with bold black lines.

7 reduced the number of tri-criteria hotspots to 74 PICS (2.68%), while threshold 8 eliminated all tri-criteria overlaps (0 PICS). Based on this analysis, threshold 7 was identified as optimal, balancing selectivity with statistical robustness. The 74 Critical Hotspots identified at this threshold exhibited mean values of proximity exposure class 9.8 (range 8–10), susceptibility class 7.0 (invariant at class 7), and mean area-wide exposure of 0.143 (range 0.128–0.172, corresponding to classes 7–9, see Supplementary Table 7 for the complete list of acronyms and their definitions).

Discussion

Our analysis of submarine canyon head retreat susceptibility along the Italian continental margins revealed the combined influence of morphological and tectonic factors in driving canyon retreat. By compiling the first nationwide high-resolution database of submarine canyon heads (2765 PICS) and employing robust multivariate regression techniques, we quantified, for the first time, the relative contributions of various drivers to submarine mass-movement susceptibility. This spatial scale of analysis

provides insights that cannot be achieved through single case studies alone. In the following, we discussed the achieved results within the framework of the entire studied area. Moreover, to examine the regional variability of canyon head retreat processes and their associated potential hazards, we also selected two focus areas along the Italian margins that have been extensively studied in previous research. These areas enable us to explore their related geohazards with a deeper understanding of the local seismotectonic and morphological context, and to validate our model against well-documented hazardous regions.

The regression analyses reveal seismogenic fault activity ($DISS_{snt}$) as the overwhelmingly dominant driver of canyon head retreat susceptibility across Italian margins. In the Huber model, $DISS_{snt}$ exhibits an exceptional contribution of 8.58×10^{16} units ($p < 0.001$), approximately nine orders of magnitude larger than the second-ranked variable ($CPTI_{15} = 2.10 \times 10^7$, $p = 0.350$) and 11 orders of magnitude larger than the distance to river mouths ($D_{Pr} = 1.10 \times 10^5$, $p < 0.001$). This extreme dominance indicates that proximity to active seismogenic sources exerts a far stronger control on canyon head instability than any other measured parameter^{8,90}. However, this finding must be contextualized within the potential dual role of seismic activity. While acting as a primary destabilizing trigger, repeated ground shaking over time can also induce 'seismic strengthening' of the seabed, which increases substrate consolidation^{80,91–93}. This competing effect could, in turn, influence (and potentially inhibit) the long-term retrogradation of SCs and warrants further investigation.

In the Stepwise model, seismic forcing maintains its primacy but operates through a different mechanism: $DISS_{snt}$ appears as the key moderating variable in the five highest-contributing interaction terms, all exceeding 10^{17} units. The dominant interactions are with hydrological parameters ($r_{FlowAcc} : DISS_{snt} = 6.37 \times 10^{18}$, $r_{Ksn} : DISS_{snt} = 2.54 \times 10^{18}$) and geodetic deformation measures ($GNSS_{inv} : DISS_{snt} = 1.70 \times 10^{18}$, $GNSS_h : DISS_{snt} = 1.28 \times 10^{18}$, $GNSS_v : DISS_{snt} = 3.36 \times 10^{17}$), all with $p < 0.01$. This pattern demonstrates that seismic forcing amplifies the influence of both sediment supply and active crustal deformation in driving canyon retreat. Specifically, seismic activity can initiate a multi-hazard cascade: it acts as a trigger for events, such as submarine landslides, on slopes already destabilized (or 'conditioned') by high sediment loads or active deformation⁹⁴.

The prominence of fault-based seismicity ($DISS_{snt}$) over catalog-based seismicity ($CPTI_{15}$) provides important mechanistic insights. While $CPTI_{15}$ shows substantial contributions in the Stepwise model through its interactions ($D_{Pr} : CPTI_{15} = 1.28 \times 10^{12}$, $p < 0.001$; $r_{Ksn} : CPTI_{15} = 3.97 \times 10^9$, $p < 0.001$), these remain several orders of magnitude below $DISS_{snt}$ -related contributions. This disparity suggests that proximity to mapped seismogenic sources, which integrate long-term tectonic loading and fault geometry, provides a more robust predictor of canyon head instability than historical earthquake occurrence alone. The seismogenic source database captures the spatial distribution of potential future ruptures more comprehensively than the historical catalog, which is limited by temporal incompleteness and magnitude detection thresholds^{95,96}.

Distance to river mouths (D_{Pr}) emerges as a noteworthy but secondary factor, with identical contributions of 1.10×10^5 units in both models ($p < 0.001$). Its role is amplified through interactions in the Stepwise model, particularly with seismic parameters ($D_{Pr} : CPTI_{15} = 1.28 \times 10^{12}$, $D_{Pr} : r_{Ksn} = 2.39 \times 10^5$) and distance ratios ($D_{Pr} : D_{Pc}/D_{Pr} = 5.15 \times 10^4$). This supports the hypothesis that many Italian SCs originated as subaerial river valleys subsequently submerged during post-glacial sea-level rise, creating paleovalleys that represent zones of weakness within the shelf-slope system²¹. The interaction structure suggests that river proximity becomes most influential when combined with seismic activity or steep topography, aligning with observations from the SE African and U.S. Atlantic margins where sea-level fluctuations and drainage extension influenced slope stability^{97,98}.

Active crustal deformation, measured through geodetic parameters ($GNSS_{inv}$, $GNSS_h$, $GNSS_v$, $EGMS_{avg}$), contributes primarily through its interactions with seismic forcing in the Stepwise model. The strongest

deformation-related interaction is $GNSS_{inv} : DISS_{snt}$ (1.70×10^{18} , $p < 0.001$), while deformation-seismicity coupling through $GNSS_{inv} : CPTI_{15}$ (1.16×10^9 , $p = 0.002$) demonstrates how these processes amplify each other's effects through dual mechanisms: direct steepening of submarine slopes and enhancement of seismic energy release in actively deforming zones. Areas experiencing rapid deformation may therefore represent hotspots where tectonic activity, seismic shaking, and morphological instability converge to drive canyon head retreat through coupled feedback mechanisms. The contribution analysis reveals substantial spatial heterogeneity in the factors driving susceptibility. While seismogenic sources ($DISS_{snt}$) dominate at the national scale, examining specific regional clusters reveals important variations in how this seismic forcing interacts with local morphological and hydrological conditions⁸⁶.

Finally, a consideration of time-scales is necessary. Our statistical model identifies active tectonics and seismicity as dominant drivers based on datasets covering a seismotectonic and morphotectonic time window. Consequently, our conclusions on canyon retreat susceptibility serve as a proxy for the dynamics that occurred within the time frame defined by the establishment of this setting.

The marked susceptibility contrast between actively deforming margins (median = 9–10) and stabilized settings (median = 2–5) demonstrates that active tectonics serves as a primary predisposing factor for canyon head retreat. The elevated susceptibility observed in reverse-faulting active orogenic belts and normal-faulting extensional belts reflects the dual role of active tectonics in promoting canyon head instability: (1) steepening of submarine slopes through vertical differential movements, which increases gravitational potential energy and reduces slope stability, and (2) seismic shaking frequency and magnitude, which serves as a primary triggering mechanism for retrogressive mass wasting events. The Calabrian subduction zone exemplifies this synergy, where compressional tectonics generates both steep bathymetric gradients and high seismicity, producing spatially uniform maximum susceptibility (median = 10, consistency = 1.0). This perfect consistency indicates that regional geodynamic forcing completely dominates local morphological variability in determining canyon retreat susceptibility. Conversely, the anomalously low susceptibility of the reverse-faulting old orogenic belt (median = 2) suggests that ancient, stabilized orogenic belts could not preserve the elevated geohazard potential of actively deforming margins.

The contrast in consistency values between different tectonic environments provides insights into the relative importance of regional versus local controls on susceptibility. High-consistency zones (≥ 0.5) indicate settings where canyon retreat processes are primarily controlled by uniform regional forcing, enabling reliable hazard prediction based on geodynamic classification alone. These zones exhibit narrow susceptibility distributions, with most PICS displaying similar retreat potential regardless of local position within the zone. Foreland basin settings exhibit the lowest consistency values (0.2–0.33), indicating that regional tectonics alone cannot explain the observed susceptibility variability. In these environments, local morphological factors, such as proximity to specific river mouths, local slope gradients, and sediment supply rates, play major roles in determining canyon head stability. The high IQR values (2–4) observed in foreland basins suggest that hazard assessment in these settings requires detailed site-specific analysis beyond regional geodynamic characterization. This spatial heterogeneity may reflect the transitional nature of foreland basins, where the interplay between flexural subsidence, sediment loading, and variable fluvial input creates complex local boundary conditions that modulate susceptibility independently of regional tectonic forcing.

The comparable median susceptibility values observed in normal-faulting extensional belts (median = 9) and reverse-faulting active orogenic belts (median = 10) indicate that both extensional and compressional active margins generate favorable conditions for canyon head instability, although through different mechanisms. These findings could have critical implications for regional hazard assessment strategies. In high-consistency geodynamic settings, susceptibility can be reliably predicted using regional tectonic classification, enabling efficient large-scale hazard mapping.

However, in low-consistency environments, such as foreland basins, hazard assessment requires integrating high-resolution local datasets, including bathymetry, sediment properties, and detailed fluvial connectivity analysis.

The Critical Hotspots identification underscores that the convergence of high geological susceptibility with elevated demographic exposure occurs in a limited subset of locations along the Italian margins (See Fig. 5). This spatial selectivity has important implications for prioritizing resource allocation in hazard mitigation strategies, enabling focused deployment of monitoring infrastructure and detailed risk assessment in areas where the potential societal impact is maximized. Optimal threshold identification for class ≥ 7 reveals that the highest risk levels across all three dimensions rarely coincide spatially. The adopted weighting approach highlights that even moderately susceptible canyon heads pose hazards when located adjacent to heavily exposed major population centers, potentially warranting more immediate intervention than highly susceptible sites located in remote areas. However, this emphasis on proximity exposure must be balanced against the recognition that catastrophic submarine landslides at highly susceptible sites can generate relatively far-field tsunami impacts affecting coastlines kilometers distant, as demonstrated by historical events, such as the 1929 Grand Banks tsunami and the 1977 Gioia Tauro landslide-tsunami^{89,90,99}.

The tri-criteria overlap frequencies at threshold ≥ 7 (74 PICs) indicate that most high-risk canyon heads are characterized by dominance of one or two factors rather than all three feature dimensions (proximity exposure + area-wide exposure + retreat susceptibility). This pattern has practical implications for hazard characterization: sites with proximity exposure + area-wide exposure overlaps represent locations where demographically exposed coastal zones are present, but susceptibility remains moderate, suggesting that hazard management should focus on population preparedness and tsunami early warning systems rather than geological monitoring (e.g., the Northern Sicilian Continental Margin^{12,14,26,32,100}). Conversely, sites with susceptibility + area-wide exposure overlaps represent geologically active zones in populated regions where detailed bathymetric monitoring and slope stability assessment should take priority to detect precursory signals of potential failures (e.g. the eastern coast of the Sicilian island near Mt. Etna Volcano and the city of Catania^{101–105}).

The overlapping of high values in the three components exhibit limited spatial covariance at their extreme values. This spatial independence can be interpreted through the controlling processes: canyon retreat susceptibility is primarily governed by geological factors, including active tectonics, seismicity, river proximity, and slope morphology over millennial timescales; proximity exposure reflects contemporary settlement patterns determined by socioeconomic factors and historical coastal development; area-wide exposure captures regional demographic distribution influenced by orography, agricultural suitability, and urban agglomeration processes. The 74 Critical Hotspots identified through the adaptive threshold approach represent priority targets for integrated monitoring strategies combining geological and demographic surveillance. These sites warrant the deployment of high-resolution repeat bathymetric surveys to detect active canyon-head retreat, the installation of seismic monitoring networks to capture earthquake-triggered slope failures, and the development of detailed tsunami inundation models calibrated to local bathymetry and coastal morphology. Equally important is the implementation of community-based preparedness programs in municipalities surrounding these hotspots, including public education on tsunami recognition and evacuation procedures and establishment of evacuation routes and safe zones^{106–109}.

The analysis of two focus areas along the Italian margins is aimed to a dual purpose: 1) it provided insights into varying classes of exposure to submarine canyon retreat-related hazards, and 2) it enabled the validation of our model against known hazardous regions as the Gioia Tauro Gulf and Ischia Island (Fig. 6). The analysis of the Gioia Tauro Gulf (Fig. 6A–C) demonstrates the robustness of the model's susceptibility component. In this critical area, the model accurately flags high canyon susceptibility, which is consistent with known historical events. This result simultaneously highlights a clear pathway for enhancement rather than a conceptual limitation. The current discrepancy, where high susceptibility does not translate

to high exposure, is directly attributable to the present exclusion of infrastructure location data (Figs. 4A, 5, and 6A). The model's approach is conceptually sound, and this specific limitation can be resolved simply by augmenting the exposure calculation with a layer detailing key infrastructure. This actively deforming region exhibits characteristic features that predispose it to submarine canyon retreat: a narrow continental shelf, steep slopes, and direct canyon-river connectivity enabling efficient sediment transfer from terrestrial sources to canyon heads¹¹⁰ (such small and seasonal rivers are also known as *fiumare* in the recent literature²⁷). These morphological conditions, coupled with high seismicity, create favorable circumstances for gravity-driven mass movements and associated coastal hazards. The canyon has a well-documented history of catastrophic failures, most notably the 1977 landslide-tsunami event^{89,111–114}. Numerical modeling demonstrated that a relatively small submarine failure (5.7 million m³) generated tsunami waves reaching 5 meters near the coast⁸⁹. Subsequent investigations revealed unstable sedimentary deposits at the canyon head, fresh detachment scarps from recent mass wasting events, and anthropogenic impacts—including bottom trawling damage and marine litter accumulation—that potentially exacerbate natural instability¹⁰. The topobathymetric swath profile perpendicular to the coastline (Fig. 6B) quantitatively illustrates the extreme morphological conditions. The profile reveals a narrow continental shelf transitioning abruptly into steep slope gradients. At approximately 14 km from the profile origin (corresponding to the immediate offshore zone), minimum slope values exhibit notable steepening. The minimum elevation profile of the canyon displays a pronounced convexity—a knickpoint characterized by an abrupt increase in slope gradient—indicating a transitional zone of enhanced susceptibility to retrogressive failure. Both cases show ideal conditions for submarine canyon instability, driven by active tectonics, high seismicity, and the resulting steep topography.

The submarine flanks of Ischia Island represent a distinct scenario where volcano-tectonic processes dominate the geohazard framework and interact with submarine canyon dynamics (Fig. 6D–F). Our model identified several high-susceptibility exposure hotspot PICs around the island, particularly along its southern and western margins (Figs. 4A and 5). The 3D visualization (Fig. 6D) reveals highly irregular submarine topography with multiple landslide scars and debris accumulations, while the swath profile (Fig. 6E) illustrates the extremely steep gradient of the island's submarine flanks. At approximately 2.5 km along the swath profile, there is a notable increase in relief energy that is compatible with landslide deposits, while, in the surroundings, the distribution of minimum elevations reveals an increase in slope angle, which, combined with locally enhanced relief energy, suggests the upstream area is likely characterized by excess topography, a condition where slopes exceed threshold stability angles^{115,116}. The high susceptibility values align with extensive documentation of past mass movement events from Mount Epomeo's flanks that could generate tsunami waves up to 5 meters high along nearby coastlines⁸⁸.

A key distinction of the Ischia case is the land-to-sea kinematic chain of the mass movements. While the Gioia Tauro case study involves primarily submarine processes, many of Ischia's most noteworthy mass movements originate on the subaerial flanks of Monte Epomeo and then continue to drive mass movement on the submarine canyon heads¹¹⁷. This scenario represents a hazard continuum spanning both terrestrial and marine environments, increasing both the complexity and potential impact of these events. The interaction among active volcanism, steep topography, and seismicity at Ischia creates a multi-hazard environment that requires specialized monitoring approaches integrating submarine and subaerial observations. This integration is particularly crucial given the island's high population density and importance as a tourist destination, where the potential impact of canyon-related tsunamis could be catastrophic.

While the models exhibit high explanatory power ($R^2 > 0.97$, Fig. 2), certain unexplained anomalies (or specific local drivers) highlight the need for future research into temporal dynamics, such as recurrence intervals and driving thresholds. As per the terrestrial landslides, time series of bathymetric data in selected high-susceptibility areas could provide crucial

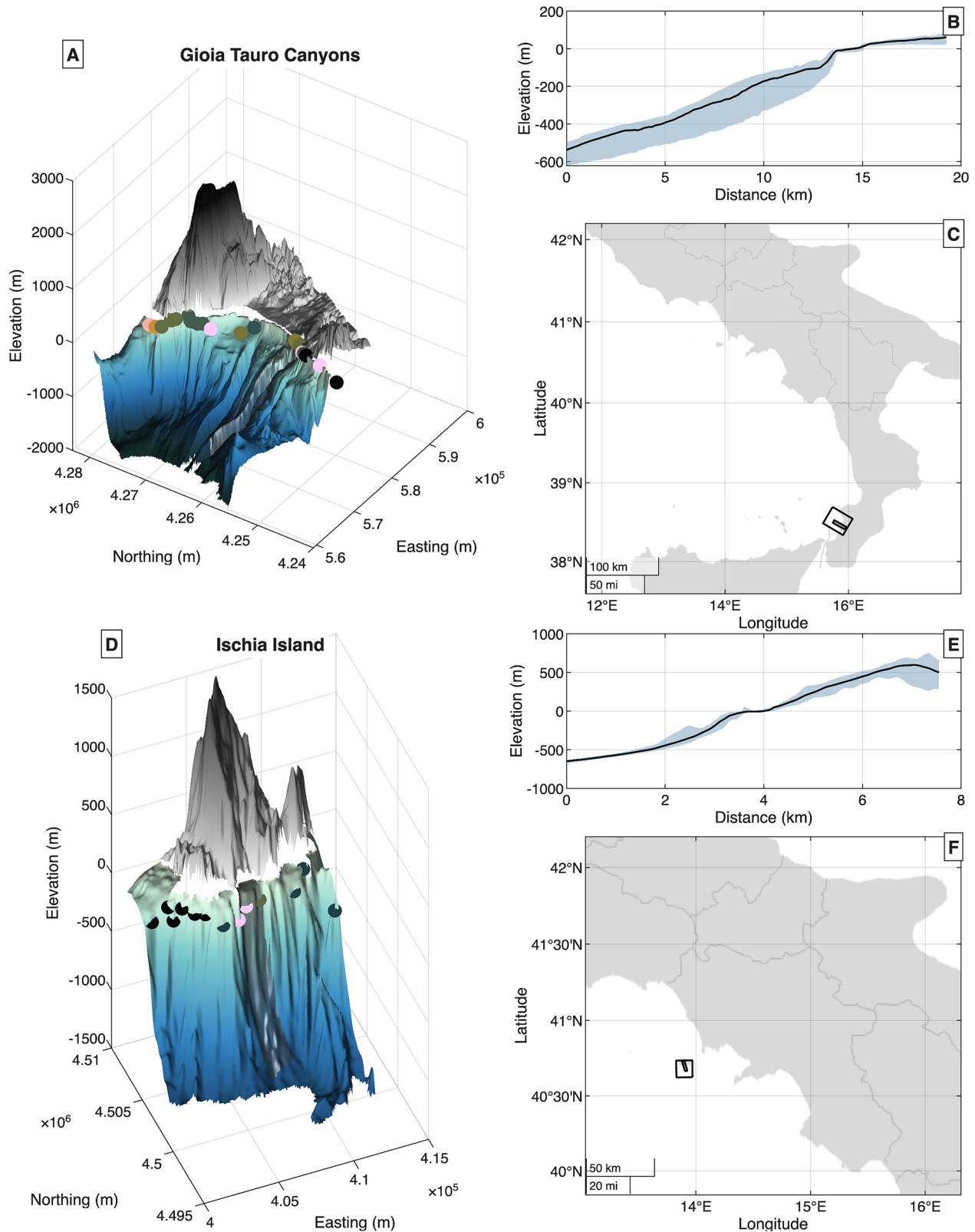


Fig. 6 | Bathymetry and swath analysis of the Gioia Tauro and Ischia Island canyon systems. 3D view of the Gioia Tauro (A) and Ischia Island (D) submarine canyon system. The small colored circles highlight the PICS location. Topobathymetry and PICS color coding are as in Fig. 3. Swath profiles of Gioia Tauro (B) and Ischia Island (E) showing elevation range in light blue and mean elevation in

black. The swath direction is perpendicular to the coastline and can be read in insets (C) and (F), respectively. Geographic context map of Gioia Tauro (C) and Ischia Island (F) showing the areas represented in the 3D visualization (larger polygon) and the swath profile corridor (smaller polygon) in relation to coastline.

insights into the rate of active processes¹¹⁸. The complex interaction effects identified in our Stepwise model suggest that canyon retreat processes are inherently non-additive, with factors, such as river proximity, seismicity, and differential tectonic deformation, acting synergically to influence susceptibility. This research supports the development of machine learning approaches to better capture these non-linear relationships¹¹⁹. The overlay of susceptibility with demographic exposure data (Fig. 4D) revealed that approximately one-third of high-susceptibility PICS coincide with densely populated coastal areas, a finding that provides important context for assessing the potential societal relevance of the hazard posed by canyon head retreat nearshore areas. Moreover, identifying previously underrecognized hazard areas, such as southeastern Sardinia, underscores the value of systematic, data-driven approaches for comprehensive hazard detection beyond traditionally recognized zones.

The contribution analysis highlights how Quaternary processes controlling the landscape evolution contribute to susceptibility conditions that may not be readily apparent when considering contemporary (e.g., historic or instrumental) tectonic activity alone. Future research should integrate onshore and offshore datasets to develop comprehensive landscape evolution models and fill the gap of no data (e.g., white ribbon), as the artificial boundary between subaerial and submarine environments has proven insufficient for understanding the complex hazard sequence of interconnected events that affect coastal regions. As demonstrated by recent studies, submarine mass movements can drive cascading hazards that propagate across the land-sea interface, affecting sediment routing systems and generating tsunamis^{86,94}. By treating the coastal zone as a continuum rather than separate domains, future investigations can more effectively address the Quaternary geological processes and associated hazards that coastal communities increasingly face, particularly in densely populated Mediterranean coastal regions and as a consequence of the sea level rise due to the global warming^{120,121}.

Conclusion

This first nationwide statistical assessment of submarine canyon head retreat susceptibility along the Italian continental margins has revealed the complex interplay between seismogenic forcing, fluvial connectivity, active deformation, and morphological factors in controlling geohazard potential. By analyzing over 2700 submarine canyon head detachment niches using a consistent methodology, we have developed a comprehensive framework that enhances our understanding and prioritization of submarine canyon-related hazards.

Among the factors investigated in this study, our analyses identify proximity to active seismogenic faults as the overwhelmingly dominant control on canyon head retreat susceptibility, exhibiting contributions approximately 9-11 orders of magnitude larger than other parameters. Distance to river mouths emerges as a secondary factor, particularly when interacting with seismic parameters and morphological variables. Regional earthquake catalog seismicity and geodetic deformation metrics primarily contribute through their interactions with these dominant factors, demonstrating that canyon retreat processes are inherently non-additive and controlled by synergistic relationships among tectonic forcing, sediment supply systems, and slope morphology.

It is important to emphasize that these findings reflect the specific set of variables analyzed in our study. Other factors documented in the literature, including sediment transport dynamics, turbidity current frequency and magnitude, dense shelf water cascading, sediment grain size distribution, and the efficiency of canyons as sediment conduits from shelf to deep basin, may exert influence on canyon evolution and retreat rates but were not directly quantified in this analysis. Future investigations integrating time-series bathymetric data with sediment-flux measurements could provide crucial insights into the rates and temporal patterns of active retrogressive processes, thereby bridging the gap between susceptibility assessment and hazard quantification.

The identification of both well-documented high-hazard regions validates our approach while highlighting the value of systematic, data-

driven hazard assessment at regional scales. The aggregation of susceptibility by seismogenic zones revealed that geodynamic setting exerts strong control on both the magnitude and spatial consistency of canyon retreat potential, with active orogenic belts and extensional margins displaying elevated and spatially uniform susceptibility.

Ongoing and future research efforts would point to investigating the relationship between submarine canyon retreat dynamics and river hydrological activity, building upon recent advances in understanding fluvial-submarine connectivity. Furthermore, new refinements of this framework could incorporate additional dimensions, including critical infrastructure exposure (ports, underwater cables, coastal defences), but also other geologically independent variables, such as the sediment dynamics and role of the SCs, to provide a more comprehensive risk prioritization tool applicable to other tectonically active coastal margins worldwide.

Data and Methods

The dataset used in this research is derived from the morpho-bathymetric database acquired as part of the MaGIC project (Marine Geohazards along the Italian Coasts¹²²), consisting of over 70,000 nautical miles of collected multibeam data. However, the dataset does not cover shallow coastal waters (due to the white ribbons problem previously mentioned) whose morpho-bathymetric mapping remains one of the primary challenges for the marine geoscience community¹²³⁻¹²⁵. Specifically, we mosaicked 68 bathymetric georeferenced raster tiles, with a geometric resolution of 50 m, imaging both the continental shelf and slope areas. Subsequently, we proceeded to map all the detachment niches within the canyon head of each SCs identified in the dataset. These features, which are the primary scars left by gravitational mass-wasting events, such as slides and slumps, were then manually outlined as a vector polyline in a georeferenced environment to precisely define their upper morphology and location (see Fig. 2).

We measured the shortest distance between each PICS and the coastline (d_{pc}), using the shoreline geodatabase developed by the Italian Institute for Environmental Protection and Research (ISPRA, LC20¹²⁶) and an in house developed code (The MathWorks Inc., 2024¹²⁷).

Morphological and Tectonic as independent Variables

Considering the d_{pc} dataset as a dependent variable, we explored different geologic processes that, as independent variables (regressors, see Table 1), may influence the susceptibility to submarine canyon retreat. The regressors considered in this study can be divided into two categories: morphological and tectonic. The morphological variables were computed using the Copernicus GLO-30 digital elevation model (30 m spatial resolution)¹²⁸, resampled to 50 m per pixel to match the spatial resolution of the bathymetric dataset and avoid computational bottlenecks (see Section 4). The resampling and some of the morphometric independent variables were computed using MATLAB¹²⁷ and the TopoToolbox library¹²⁹.

We used six morphological variables. 1) The distance between each PICS and the nearest river mouth (d_{pr}), where the geographic locations of the river mouths along the entire Italian hydrographic network (RNDD, ISPRA¹³⁰) were obtained by intersecting the drainage network with the LC20. 2) The degree of alignment between the PICS and river mouths along the line of minimum distance, computed as the ratio d_{pc}/d_{pr} . 3) The newly computed stream network flow accumulation value of the river mouth closest to each PICS ($r_{FlowAcc}$). 4) The newly computed stream network averaged normalized channel steepness index value¹³¹ of the river mouth closest to each PICS (r_{Ksn}). 5) A relief metric (RM) that was computed as the arithmetic mean of relief and topographic variance (Eq. 1), giving equal weight to both components, where relief represents the elevation difference within a moving window and topographic variance quantifies the standard deviation of elevation values within the same window:

$$RM = \frac{\left(\frac{\text{relief} - \min(\text{relief})}{\max(\text{relief}) - \min(\text{relief})} \right) + \left(\frac{\text{variance} - \min(\text{variance})}{\max(\text{variance}) - \min(\text{variance})} \right)}{2} \quad (1)$$

Relief and variance values were extracted from the bathymetry within a circular area with a 4000 m radius, centered on each PICS. 6) The slope value (s) computed in the PICS location.

Among the tectonic independent variables are crustal deformation proxies as 26 years of GNSS positioning data from about 920 continuous GNSS stations, spanning the 1994/2020-time interval from several geodetic networks evenly distributed across the Italian territory (see supplementary notes for details). The raw data processing followed the workflow proposed by Palano et al.¹³² (see Supplementary Information for further details on GNSS processing, Supplementary Note 1) and allowed the computation of horizontal and vertical velocity fields (numbered 7 and 8, labeled GNSS_v, GNSS_h, respectively). Moreover, we computed the 2nd invariance of the horizontal strain rate values, a scalar metric that quantifies the total magnitude of deformation, thereby identifying zones undergoing intense deformation and to distinguish regions dominated by compressional or extensional regimes, numbered 9 and labeled GNSS_{2inv}.

We also considered the vertical ground movements measured by Sentinel-1 data along the coastline analyzed using Synthetic Aperture Radar Interferometry (InSAR), and freely available in the European Ground Motion Service^{133,134}. Specifically, we used the vertical displacements from the Level 3 Ortho product, with a spatial resolution of approximately 100 by 100 m. To provide an averaged assessment for the area surrounding each PICS, such a metric was calculated by averaging the ground motion values from the 10 InSAR points closest to each PICS within a 4 km search radius (numbered 10 and labeled EGMS_{avg}). To consider the long-term vertical deformation, we used uplift rates computed from elevation of MIS 5.5 paleoshorelines, reported in the literature¹³⁵ (labeled F₀₆, see Supplementary Note 2).

We quantified earthquake density around each PICS location using a custom MATLAB function that computes density values within circular buffers of variable radii. Following Burrato et al.^{136,137}, buffer radii were defined according to the 95th percentile of epicentral distances corresponding to landslide occurrences: 41.5 km for Mw < 5.5, 66.3 km for 5.5 ≤ Mw < 6.5, and 77.3 km for Mw ≥ 6.5. Rather than computing simple earthquake counts, we implemented a seismic moment-weighted density approach. For each earthquake within the buffer, we calculated the scalar seismic moment (that correlates directly with radiated seismic energy and resultant ground motion parameters¹³⁸) using the standard relationship:

$$M_0 = 10^{1.5M_w + 10.7} N \backslash m \tag{2}$$

The density value at each PICS location was then computed as:

$$\rho_{eq} = \frac{\sum M_{0,i}}{\pi r^2} \tag{3}$$

where the summation includes all earthquakes *i* falling within the buffer radius *r*. This approach provides a physically based measure that reflects actual seismic energy release rather than simple event counts, better representing the cumulative ground-shaking potential. We applied this calculation to two independent earthquake datasets: the Italian parametric earthquake catalog (numbered 12 and labeled CPTI₁₅) and a dataset of synthetic epicenters (numbered 13 and labeled DISS_{snt}). The first one includes 1766 historical and instrumental events with Mw ≥ 4.0 covering the time period from the year 1000 to 2020 (CPTI15v4.0¹³⁹). The second one consists of 2,354 scenario earthquakes (M > 5.5) generated using a floating fault approach¹⁴⁰ along the Composite Seismogenic Sources (CSS) of the DISS database¹⁴¹. Synthetic hypocentres were positioned at 2/3 of the CSS width depth and distributed at 5-km intervals along-strike.

Data Preprocessing and Transformation

To investigate the relationships between PICS locations and the various selected regressors, we implemented a comprehensive statistical analysis framework focused on understanding how different independent variables

impact the d_{pc} value. In doing this, we assumed the PICS–coast distance as a proxy for the susceptibility to retrogressive canyon evolution, where a shorter distance indicates higher susceptibility to the retreat of individual detachment niches. Given the incompleteness the employed datasets, we first addressed the issue of missing values in our input variables through linear interpolation, ensuring data continuity without introducing artificial patterns. Given the typically skewed nature of distance measurements in geological contexts, we applied a Box-Cox transformation to d_{pc}, aiming to normalize its distribution and stabilize variance¹⁴². To account for differences in scales between independent variables and to improve the interpretability of regression coefficients, we standardized each variable using the Z-score method¹⁴³. For each independent variable, both standardized and non-standardized, we systematically tested linear, logarithmic, square root, quadratic, and exponential transformations to identify the optimal mathematical approach for linearization. We evaluated each transformation's effectiveness using coefficient of determination (R²) values, AIC, and BIC, selecting the transformation that best captured the underlying relationships while maintaining interpretability¹⁴⁴ (Supplementary Table 1).

Multiple Linear Regression Analysis

We used the linearized regressors as input datasets for a regression analysis that employed two complementary approaches to ensure robust results. Firstly, we implemented a stepwise regression with bidirectional elimination, which systematically evaluated the significance of each regressor and their combination while controlling for the influence of other variables^{145,146}. This method allowed us to identify the most important regressors affecting

d_{pc} values while avoiding overparameterization of the overall model. In parallel, we applied a Huber's robust regression, which provides more reliable results in the presence of outliers or when the data doesn't perfectly meet classical regression assumptions, such as the heteroscedasticity in the distribution of the residuals¹⁴⁷. The performance of both multiple linear regression models (Stepwise and Huber) was evaluated using R² and its adjusted version, AIC, BIC, the RMSE and MAE, measuring the average prediction error (see Supplementary Table 2). Both models were validated using 5-fold cross-validation, dividing our dataset into training and testing subsets to ensure the models' predictive capabilities weren't overfitted to our specific dataset¹⁴⁸.

Model Diagnostics

We conducted a thorough investigation of regression assumptions to ensure the validity of our statistical inferences. Multicollinearity among predictor variables was assessed using VIF, with values above 5 indicating potential concerns about variable independence¹⁴⁹. To evaluate the consistency of error variance across predictions (homoscedasticity), we employed both White's test and the Breusch-Pagan test^{150,151}. The normality of residuals was assessed through both graphical QQ and numerical methods, such as Kolmogorov-Smirnov and Anderson-Darling tests^{152,153}. Where heteroscedasticity was detected, we applied White's robust standard errors to ensure valid statistical inference despite violation of classical assumptions. We conducted outlier detection using a dual approach based on residual analysis and QQ plots. For the residual analysis, we employed the IQR, where outliers were identified as points falling outside the boundaries defined for both fitted values and residuals by:

$$\text{Outliers} < Q1 - 1.5 \times \text{IQR} \tag{3}$$

$$\text{Outliers} > Q3 + 1.5 \times \text{IQR} \tag{4}$$

where Q1 and Q3 are the first and third quartiles, respectively. In the QQ plot analysis, an approach was used that classified points more than 2 standard deviations from the mean as outliers. For positive quantiles, we applied an even more conservative threshold of 1.5 standard deviations to ensure robust outlier detection. This dual methodology was applied to both the stepwise and Huber regression models to ensure comprehensive outlier identification.

Susceptibility Assessment

The final phase of our analysis involved developing a quantitative metric for assessing canyon retreat susceptibility. Using the regression results, we created a composite index that includes only those predictors found to be statistically meaningful in both regression models, with each variable weighted according to its relative importance in explaining the response variable. The susceptibility index (S_i) for each location i was calculated as:

$$S_i = \sum_{j=1}^n \beta_j X_{ij} \tag{5}$$

where:

- β_j is the standardized coefficient (from White’s robust estimation) for predictor j ;

- X_{ij} is the value of predictor j at location i ;
 - n is the number of meaningful predictors in the model.
- For any interaction terms present in the model, the equation expands to:

$$S_i = \sum_{j=1}^p \beta_j X_{ij} + \sum_{k=1}^q \beta_k (X_{im} \times X_{in}) \tag{6}$$

where:

- p is the number of individual predictors;
- q is the number of interaction terms;
- X_{im} and X_{in} are the interacting variables;
- β_k is the coefficient for the interaction term.

More explicitly, if we consider all the meaningful variables in our model, the equation becomes:

$$S_i = \beta_1 (d_{Pr})_i + \beta_2 (d_{PrC})_i + \beta_n (\dots)_i \dots \tag{7}$$

This formulation excludes the intercept term (β_0) as we are interested in the relative contributions of the predictors rather than absolute values. We calculated this susceptibility index using coefficients from both the stepwise regression and Huber regression models, allowing us to compare and validate the results across different statistical approaches. The weights (β_j) were derived from standardized regression coefficients to ensure that variables measured in different units could be meaningfully combined into a single metric.

The statistical significance of each predictor was assessed through p -values calculated using White’s heteroscedasticity-consistent standard errors. P -values lower than 0.05 were considered statistically meaningful. Extremely small p -values ($<1e-16$) were rounded to zero in the output, indicating major contributions. The contribution of each variable or interaction term to the overall susceptibility was then quantified as the absolute value of the mean effect across all locations:

$$C_j = \left| \frac{1}{N} \sum_{i=1}^N \beta_j X_{ij} \right| \tag{8}$$

where C_j is the contribution of predictor j , N is the total number of locations, β_j is the coefficient, and X_{ij} represents either a single variable or the product of two variables in the case of interaction terms. This metric provides a measure of the average magnitude of each predictor’s effect on the susceptibility index, allowing for the ranking of variables by their relative importance in the model.

To classify submarine canyon head retreat susceptibility, we employed a quantile-based approach that preserved the inherent statistical distribution of the values and utilized chi-square tests for validation. The resulting categories were then assigned descriptive labels ranging from ‘Very Low’ to ‘Critical’, facilitating a qualitative interpretation of the results.

Susceptibility Aggregation by Geodynamic Setting

To investigate the relationship between submarine canyon head retreat susceptibility and regional seismotectonic conditions, we aggregated PICS-level susceptibility values within the seismogenic zones defined by the Italian Seismogenic Zonation (ZS16)^{45,46}. Each PICS was spatially assigned to its corresponding ZS16 zone using a point-in-polygon analysis, enabling the characterization of susceptibility patterns across different fault kinematic regimes (e.g., normal, reverse, strike-slip, and undefined) and geodynamic settings (e.g., orogenic belts, foreland basins, back-arc basins, extensional belts). For each seismogenic zone containing at least three PICS, we computed descriptive statistics of the susceptibility distribution: mean, median, 25th percentile (P25), 75th percentile (P75), interquartile range (IQR = P75 – P25), minimum, and maximum values. To quantify the spatial homogeneity of susceptibility within each zone—reflecting the degree to which geodynamic forcing uniformly controls canyon head retreat processes—we defined a consistency metric as:

$$\text{Consistency} = \frac{1}{1 + \text{IQR}} \tag{9}$$

This metric ranges from 0 (highly heterogeneous susceptibility, indicating complex multi-factor control) to 1 (spatially uniform susceptibility, suggesting dominant tectonic forcing). To facilitate comparative visualization, median susceptibility values were linearly normalized to a 0–1 range. Since median values span from 1 (minimum observed susceptibility) to 10 (maximum observed susceptibility), the normalization was performed using:

$$\text{Normalized Median} = \frac{\text{Median} - 1}{9} \tag{10}$$

Relating Susceptibility to Coastal Demographic Exposure

We conducted a multi-criteria analysis examining the spatial correlation between PICS susceptibility and demographic exposure (ISTAT¹⁵⁴ census data) along the Italian coastline. Such demographic exposure was computed as a multiplicative index of four normalized (0–100) and quantile-classified parameters: population density, elevation, municipal area, and coastal distance. A Boolean weighting scheme was applied to elevation to restrict the exposure assessment to the most vulnerable coastal areas. Maximum weight was allocated solely to municipalities bordering the coastline or those situated within the lowest decile (10%) of mean elevation. Moreover, we computed two complementary exposure metrics for each PICS, the first, proximity exposure, quantifies the maximum demographic pressure in the immediate vicinity of each canyon head by identifying the highest demographic value among municipalities whose vertices fell within 10% of the minimum distance to the PICS, ensuring capture of severe exposure scenarios while maintaining spatial coherence. The second metric, area-wide exposure, quantifies the cumulative demographic pressure across a broader coastal zone by computing the weighted average of all municipal exposure values within a 10 km buffer around each PICS, with weights following an exponential distance-decay function to emphasize proximal municipalities. The 10 km buffer distance was established based on the most recent literature concerning the effects of local tsunamis generated by nearshore submarine mass failures mostly in the Mediterranean area^{155–163}. This area-wide metric is incorporated into the integrated tsunami-landslide exposure index. This index is formulated by combining coastal population exposure with the computed susceptibility, the latter serving as a proxy for seafloor slope instability potential. Both exposure metrics were classified into 10 quantile-based classes across the entire PICS dataset (class 1 = lowest exposure, class 10 = highest exposure).

To integrate the multi-dimensional risk information into a unified priority metric, we developed a composite risk score combining three normalized components: canyon retreat susceptibility, proximity exposure, and the integrated tsunami-landslide exposure. The composite priority

score was then calculated as a weighted linear combination:

$$\text{Priority Score} = 100 \times [(0.40 \times E_{\text{prox}}) + (0.30 \times S_{\text{norm}}) + (0.30 \times E_{\text{area}})] \quad (11)$$

where E_{prox} represents normalized proximity exposure, S_{norm} represents normalized canyon retreat susceptibility, and E_{area} represents the normalized area-wide exposure component. The weighting scheme (40% proximity exposure, 30% susceptibility, 30% area-wide exposure) prioritizes immediate local exposure while maintaining balanced consideration of geological susceptibility and broader regional exposure patterns.

Finally, to identify canyon heads requiring immediate attention in hazard mitigation strategies, we implemented a Priority Score adaptive threshold approach testing multiple class-based criteria (≥ 6 , ≥ 7 , ≥ 8 , ≥ 9) applied simultaneously to all three criticality components. The optimal threshold was determined as the most restrictive criterion yielding a statistically meaningful number of multi-criteria hotspots (≥ 7). A PICS was classified as a Critical Hotspot if it satisfied all three conditions simultaneously: proximity exposure class \geq threshold, susceptibility class \geq threshold, and area-wide class \geq threshold. Critical Hotspots were marked with distinct symbols to distinguish multi-criteria priority sites from the broader PICS population.

Data availability

The datasets analyzed during the current study are available in the following public repositories: Bathymetric data: Github page of MaGIC project (<https://github.com/pcm-dpc/MaGIC.git>); Seismogenic sources (DISS): Istituto Nazionale di Geofisica e Vulcanologia (<http://diss.rm.ingv.it/diss/>); Historical seismicity (CPT115): INGV DBMI15; Ground deformation (EGMS): Copernicus Land Monitoring Service (<https://egms.land.copernicus.eu/>). All other data supporting the findings of this study are available within the article and its Supplementary Information.

Received: 19 March 2025; Accepted: 26 February 2026;

Published online: 12 March 2026

References

- Shepard, F. P. Submarine canyons. *Earth-Sci. Rev.* **8**, 1–12 (1972).
- Canals, M. et al. Flushing submarine canyons. *Nature* **444**, 354–357 (2006).
- Harris, P. T. & Whiteway, T. Global distribution of large submarine canyons: geomorphic differences between active and passive continental margins. *Mar. Geol.* **285**, 69–86 (2011).
- Chiocci, F. L. & Ridente, D. Regional-scale seafloor mapping and geohazard assessment. The experience from the Italian project MaGIC (Marine Geohazards along the Italian Coasts). *Mar. Geophys. Res.* **32**, 13–23 (2011).
- Lo Iacono, C. et al. Submarine canyon morphologies in the Gulf of Palermo (Southern Tyrrhenian Sea) and possible implications for geo-hazard. *Mar. Geophys. Res.* **32**, 127–138 (2011).
- Lo Iacono, C., Sulli, A. & Agate, M. Submarine canyons of north-western Sicily (Southern Tyrrhenian Sea): Variability in morphology, sedimentary processes and evolution on a tectonically active margin. *Deep Sea Res. Part II: Topical Stud. Oceanogr.* **104**, 93–105 (2014).
- Hampton, M. A., Lee, H. J. & Locat, J. Submarine landslides. *Rev. Geophys.* **34**, 33–59 (1996).
- Ceramicola, S. et al. Submarine Mass-Movements Along the Slopes of the Active Ionian Continental Margins and Their Consequences for Marine Geohazards (Mediterranean Sea). In *Submarine Mass Movements and Their Consequences: 6th International Symposium* (eds Krastel, S. et al.) 295–306 https://doi.org/10.1007/978-3-319-00972-8_26 (Springer International Publishing, Cham, 2014).
- Bernhardt, A. et al. Controls on submarine canyon activity during sea-level highstands: the Biobío canyon system offshore Chile. *Geosphere* **11**, 1226–1255 (2015).
- Pierdomenico, M., Martorelli, E., Dominguez-Carrió, C., Gili, J. M. & Chiocci, F. L. Seafloor characterization and benthic megafaunal distribution of an active submarine canyon and surrounding sectors: the case of Gioia Canyon (Southern Tyrrhenian Sea). *J. Mar. Syst.* **157**, 101–117 (2016).
- Srivastava, E. et al. Extremely fast Holocene coastal landscape evolution in the Kachchh Upland (NW India): clues from a multidisciplinary review. *J. Maps* **19**, 2167617 (2023).
- Agate, M. et al. Decoding Late Quaternary faulting through marine terraces and MIS 5.5 tilted tidal notches: Insights from central Mediterranean Sea (NW Sicily, Italy). *Geomorphology* **472**, 109587 (2025).
- Caldareri, F. et al. On the shoreline monitoring via earth observation: an isoradiometric method. *Remote Sens. Environ.* **311**, 114286 (2024).
- Parrino, N. et al. Elusive active faults in a low strain rate region (Sicily, Italy): hints from a multidisciplinary land-to-sea approach. *Tectonophysics* **839**, 229520 (2022).
- Parrino, N. et al. Plio-Quaternary coastal landscape evolution of north-western Sicily (Italy). *J. Maps* **19**, 2159889 (2023).
- Pirrota, C., Parrino, N., Pepe, F., Tansi, C. & Monaco, C. Geomorphological and morphometric analyses of the catanzaro trough (Central Calabrian Arc, Southern Italy): seismotectonic implications. *Geosciences* **12**, 324 (2022).
- Malik, J. N. et al. Holocene surface-rupturing paleo-earthquakes along the Kachchh Mainland Fault: shaping the seismic landscape of Kachchh, Western India. *Sci. Rep.* **14**, 11612 (2024).
- Maltese, A. et al. On the shoreline positioning via remote sensing imagery: an isoradiometric approach. *J. Appl. Rem. Sens.* **18**, <https://doi.org/10.1117/1.JRS.18.014529> (2024).
- Canals, M. et al. The Ebro Continental Margin, Western Mediterranean Sea: interplay between canyon-channel systems and mass wasting processes. In *Deep-Water Reservoirs of the World* (ed. Weimer, P.) vol. 200 (SEPM Society for Sedimentary Geology, 2000).
- Baztan, J. et al. Axial incision: The key to understand submarine canyon evolution (in the western Gulf of Lion). *Mar. Pet. Geol.* **22**, 805–826 (2005).
- Bernhardt, A. & Schwanghart, W. Where and why do submarine canyons remain connected to the shore during sea-level rise? Insights from global topographic analysis and Bayesian Regression. *Geophys. Res. Lett.* **48**, e2020GL092234 (2021).
- Ceramicola, S. et al. Geohazard features of the Gulf of Taranto. *J. Maps* **20**, 2431073 (2024).
- Ceramicola, S. et al. *Submarine Canyon Dynamics in the Mediterranean and Tributary Seas - An Integrated Geological, Oceanographic and Biological Perspective*, ISSN 1726-5886 (CIESM, 2015).
- Migeon, S. et al. Morphology, distribution and origin of recent submarine landslides of the Ligurian Margin (North-western Mediterranean): some insights into geohazard assessment. *Mar. Geophys. Res.* **32**, 225–243 (2011).
- Ceramicola, S., Praeg, D., Cova, A., Accettella, D. & Zecchin, M. Seafloor distribution and last glacial to postglacial activity of mud volcanoes on the Calabrian accretionary prism, Ionian Sea. *Geo-Mar. Lett.* **34**, 111–129 (2014).
- Caldareri, F. et al. Shoreline time series analysis through the Isoradiometric method: bridging landscape evolution and coastal management. *Int. J. Appl. Earth Observ. Geoinf.* **141**, <https://doi.org/10.1117/1.JRS.18.014529> (2025).
- Ceramicola, S. et al. Geohazard Features of the Ionian Calabrian Margin. *J. Maps* **20**, 2349785 (2024).
- Lo Iacono, C. et al. Large, deepwater slope failures: implications for landslide-generated tsunamis. *Geology* **40**, 931–934 (2012).
- Sulli, A. et al. Submarine Slope Failures Along the Northern Sicilian Continental Margin (Southern Tyrrhenian Sea) and Possible Implications for Geo-Hazard. in *Landslide Science and Practice:*

- Volume 5: *Complex Environment* (eds Margottini, C., Canuti, P. & Sassa, K.) 41–48 (Springer, 2013). https://doi.org/10.1007/978-3-642-31427-8_5.
30. Sulli, A., Agate, M., Zizzo, E., Gasparo Morticelli, M. & Lo Iacono, C. Geo-hazards of the San Vito peninsula offshore (southwestern Tyrrhenian Sea). *J. Maps* **17**, 185–196 (2021).
 31. Casalbore, D., Romagnoli, C., Bosman, A., Anzidei, M. & Chiocci, F. L. Coastal hazard due to submarine canyons in active insular volcanoes: examples from Lipari Island (southern Tyrrhenian Sea). *J. Coast Conserv* **22**, 989–999 (2018).
 32. Lo Presti, V. et al. Geohazard assessment of the north-eastern Sicily continental margin (SW Mediterranean): coastal erosion, sea-level rise and retrogressive canyon head dynamics. *Mar. Geophys Res.* **43**, 2 (2022).
 33. Bernhardt, A. & Schwanghart, W. Seafloor slopes control submarine canyon distribution: A global analysis. *Sci. Adv.* <https://doi.org/10.1126/sciadv.adv3942> (2025).
 34. Bührig, L. H., Colombera, L., Patacci, M., Mountney, N. P. & McCaffrey, W. D. A global analysis of controls on submarine-canyon geomorphology. *Earth-Sci. Rev.* **233**, 104150 (2022).
 35. Stiftung, B. Sustainable governance indicators 2011. *Gütersloh: Bertelsmann* https://www.digitale-schule-t.de/fileadmin/files/BSt/Publikationen/imported/leseprobe/LP_978-3-86793-394-0_1.pdf (2011). ISBN:978-3-86793-394-0
 36. Vesperini, G. Regional and local government in Italy: an overview. *SSRN Sch. Pap.* <https://doi.org/10.2139/ssrn.1332762> (2009).
 37. Barbano, A. et al. *Proposta Metodologica per l'aggiornamento Delle Mappe Di Pericolosità e Di Rischio - Attuazione Della Direttiva 2007/60/CE Relativa Alla Valutazione e Alla Gestione Dei Rischi Da Alluvioni (Decreto Legislativo n.49/2010)*. ISBN: 978-88-448-0571-5 (2013).
 38. Hauer, M. E. et al. Assessing population exposure to coastal flooding due to sea level rise. *Nat. Commun.* **12**, 6900 (2021).
 39. Tavani, S. et al. Zipper tectonics in the Tyrrhenian-Apennines system: linking rift inheritance with thrusting, back-arc extension and crustal delamination. *Earth-Sci. Rev.* **271**, 105305 (2025).
 40. Dewey, J. F., Helman, M. L., Knott, S. D., Turco, E. & Hutton, D. H. W. Kinematics of the western Mediterranean. *SP* **45**, 265–283 (1989).
 41. Faccenna, C. et al. Mantle dynamics in the mediterranean: mediterranean dynamic. *Rev. Geophys.* **52**, 283–332 (2014).
 42. Malinverno, A. & Ryan, W. B. F. Extension in the Tyrrhenian Sea and shortening in the Apennines as result of arc migration driven by sinking of the lithosphere. *Tectonics* **5**, 227–245 (1986).
 43. Wortel, M. J. R. & Spakman, W. Subduction and slab detachment in the mediterranean-carpethian region. *Science* **290**, 1910–1917 (2000).
 44. Maiorana, M. et al. Is the sicily channel a simple rifting zone? New evidence from seismic analysis with geodynamic implications. *Tectonophysics* **864**, 230019 (2023).
 45. Visini, F. et al. An updated area-source seismogenic model (MA4) for seismic hazard of Italy. *Nat. Hazards Earth Syst. Sci.* **22**, 2807–2827 (2022).
 46. Pondrelli, S. et al. Style of faulting of expected earthquakes in Italy as an input for seismic hazard modeling. *Nat. Hazards Earth Syst. Sci.* **20**, 3577–3592 (2020).
 47. Serpelloni, E. et al. Surface velocities and strain-rates in the euro-mediterranean region from massive gps data processing. *Front. Earth Sci.* **10**, 907897 (2022).
 48. Buttinelli, M. et al. Tectonic-SEDIMENTARY evolution of the Tuscan shelf (Italy): Seismic-stratigraphic/structural analysis of Neogenic succession in the Tyrrhenian Sea between Elba Island and Monte Argentario promontory. *Tectonophysics* **873**, 230211 (2024).
 49. Faccenna, C., Becker, T. W., Lucente, F. P., Jolivet, L. & Rossetti, F. History of subduction and back arc extension in the Central Mediterranean. *Geophys J. Int.* **145**, 809–820 (2001).
 50. Chiarabba, C., Buttinelli, M., Cattaneo, M. & De Gori, P. Large earthquakes driven by fluid overpressure: the apennines normal faulting system Case. *Tectonics* **39**, e2019TC006014 (2020).
 51. Polonia, A. et al. The Calabrian Arc subduction complex in the Ionian Sea: Regional architecture, active deformation, and seismic hazard. *Tectonics* **30**, <https://doi.org/10.1029/2010TC002821> (2011).
 52. Neri, G., Barberi, G., Orecchio, B. & Mostaccio, A. Seismic strain and seismogenic stress regimes in the crust of the southern Tyrrhenian region. *Earth Planet. Sci. Lett.* **213**, 97–112 (2003).
 53. Selvaggi, G. & Chiarabba, C. Seismicity and P-wave velocity image of the Southern Tyrrhenian subduction zone. *Geophys. J. Int.* **121**, 818–826 (1995).
 54. Corradino, M. et al. An integrated multiscale method for the characterisation of active faults in offshore areas. The case of Sant'Eufemia Gulf (Offshore Calabria, Italy). *Front. Earth Sci.* **9**, 670557 (2021).
 55. Finetti, I. R. & Del Ben, A. Crustal tectono-stratigraphic setting of the Adriatic Sea from new CROP seismic data. *CROP Proj. Deep Seismic Explor. Cent. Mediterranean Italy* **1**, 519–548 (2005).
 56. Civile, D. et al. The Pantelleria graben (Sicily Channel, Central Mediterranean): an example of intraplate 'passive'rift. *Tectonophysics* **490**, 173–183 (2010).
 57. Corti, G., Cuffaro, M., Doglioni, C., Innocenti, F. & Manetti, P. Coexisting geodynamic processes in the Sicily Channel. [https://doi.org/10.1130/2006.2409\(05\)](https://doi.org/10.1130/2006.2409(05)) (2006).
 58. Barrea, G. et al. Geodetic and geological evidence of active tectonics in south-western Sicily (Italy). *J. Geodynam.* **82**, 138–149 (2014).
 59. Neri, G., Orecchio, B., Totaro, C., Falcone, G. & Presti, D. Subduction beneath southern Italy close the ending: results from seismic tomography. *Seismol. Res. Lett.* **80**, 63–70 (2009).
 60. Maesano, F. E., Tiberti, M. M. & Basili, R. The Calabrian Arc: three-dimensional modelling of the subduction interface. *Sci. Rep.* **7**, 8887 (2017).
 61. Antonoli, F. et al. The last interglacial transgression in Italy: the breath of the Italian coasts documented by 461 sites. *Quat. Sci. Rev.* **360**, 109376 (2025).
 62. Westaway, R. Quaternary uplift of southern Italy. *J. Geophys. Res. Solid Earth* **98**, 21741–21772 (1993).
 63. Orecchio, B., Neri, G., Presti, D., Scolaro, S. & Totaro, C. Seismic deformation styles in the upper and lower plate domains of the Calabrian subduction zone, south Italy. *J. Geodynam.* **145**, 101847 (2021).
 64. Pondrelli, S. et al. The Italian CMT dataset from 1977 to the present. *Phys. Earth Planet. Inter.* **159**, 286–303 (2006).
 65. Branca, S. & Ferrara, V. The morphostructural setting of Mount Etna sedimentary basement (Italy): implications for the geometry and volume of the volcano and its flank instability. *Tectonophysics* **586**, 46–64 (2013).
 66. De Astis, G., Ventura, G. & Vilardo, G. Geodynamic significance of the Aeolian volcanism (Southern Tyrrhenian Sea, Italy) in light of structural, seismological, and geochemical data. *Tectonics* **22**, 2003TC001506 (2003).
 67. Global Volcanism Program & Venzke, E. Volcanoes of the World, v.5.3.1. Global Volcanism Program. <https://doi.org/10.5479/si.GVP.VOTW5-2025.5.3> (2025).
 68. Amblas, D. et al. Submarine Canyons. in *Treatise on Geomorphology* 830–846 (Elsevier, 2022). <https://doi.org/10.1016/B978-0-12-818234-5.00146-2>.
 69. Amblas, D. et al. Submarine Canyons and Gullies. in *Submarine Geomorphology* (eds Micallef, A., Krastel, S. & Savini, A.) 251–272 (Springer International Publishing, 2018). https://doi.org/10.1007/978-3-319-57852-1_14.
 70. Li, S. et al. Morphology and evolution of submarine canyons on the northwest South China Sea margin. *Mar. Geol.* **443**, 106695 (2022).

71. Tubau, X. et al. Submarine canyons of Santa Monica Bay, Southern California: variability in morphology and sedimentary processes. *Mar. Geol.* **365**, 61–79 (2015).
72. Jobe, Z. R., Lowe, D. R. & Uchytel, S. J. Two fundamentally different types of submarine canyons along the continental margin of Equatorial Guinea. *Mar. Pet. Geol.* **28**, 843–860 (2011).
73. Almeida, N. M. de, Vital, H. & Gomes, M. P. Morphology of submarine canyons along the continental margin of the Potiguar Basin, NE Brazil. *Mar. Pet. Geol.* **68**, 307–324 (2015).
74. Gerber, T. P., Amblas, D., Wolinsky, M. A., Pratson, L. F. & Canals, M. A model for the long-profile shape of submarine canyons. *J. Geophys. Res. Earth Surface* **114**, <https://doi.org/10.1029/2008JF001190> (2009).
75. Twichell, D. C. & Roberts, D. G. Morphology, distribution, and development of submarine canyons on the United States Atlantic continental slope between Hudson and Baltimore Canyons. *Geology* **10**, 408–412 (1982).
76. Harris, P. T., Macmillan-Lawley, M., Rupp, J. & Baker, E. K. Geomorphology of the oceans. *Mar. Geol.* **352**, 4–24 (2014).
77. *Submarine Geomorphology*. (Springer International Publishing, 2018). <https://doi.org/10.1007/978-3-319-57852-1>.
78. Soutter, E. L., Kane, I. A., Hodgson, D. M. & Flint, S. The concavity of submarine canyon longitudinal profiles. *J. Geophys. Res. Earth Surf.* **126**, e2021JF006185 (2021).
79. Covault, J. A., Fildani, A., Romans, B. W. & McHargue, T. The natural range of submarine canyon-and-channel longitudinal profiles. *Geosphere* **7**, 313–332 (2011).
80. Bührig, L. H., Colombera, L., Patacci, M., Mountney, N. P. & McCaffrey, W. D. Tectonic influence on the geomorphology of submarine canyons: implications for deep-water sedimentary systems. *Front. Earth Sci.* **10**, <https://doi.org/10.3389/feart.2022.836823> (2022).
81. Lahr, E. J., Ogston, A. S., Hill, J. C., Glover, H. E. & Rosenberger, K. J. Submarine canyon sediment transport and accumulation during sea level highstand: Interactive seasonal regimes in the head of Astoria Canyon, WA. *Mar. Geol.* **484**, 107516 (2025).
82. Allen, S. E. & Durrieu de Madron, X. A review of the role of submarine canyons in deep-ocean exchange with the shelf. *Ocean Sci.* **5**, 607–620 (2009).
83. Talling, P. eterJ., Paull, C. K. & Piper, D. J. W. How are subaqueous sediment density flows triggered, what is their internal structure and how does it evolve? Direct observations from monitoring of active flows. *Earth-Sci. Rev.* **125**, 244–287 (2013).
84. Adema, P. H. et al. Submarine channel shape controls combined turbidity current–contour current flow. *Mar. Geol.* **490**, 107646 (2025).
85. Kunath, P. et al. Ocean-bottom seismometers reveal surge dynamics in Earth’s longest-runout sediment flows. *Commun. Earth Environ.* **6**, 147 (2025).
86. Pope, E. L. et al. Carbon and sediment fluxes inhibited in the submarine Congo Canyon by landslide-damming. *Nat. Geosci.* **15**, 845–853 (2022).
87. Pohl, F., Eggenhuisen, J. T., Kane, I. A. & Clare, M. A. Transport and burial of microplastics in deep-marine sediments by turbidity currents. *Environ. Sci. Technol.* **54**, 4180–4189 (2020).
88. Zaniboni, F., Pagnoni, G., Gallotti, G., Tinti, S. & Armigliato, A. Landslide-tsunamis along the flanks of Mount Epomeo, Ischia: propagation patterns and coastal hazard for the Campania Coasts, Italy. *SP* **519**, 89–105 (2024).
89. Zaniboni, F., Armigliato, A., Pagnoni, G. & Tinti, S. Continental margins as a source of tsunami hazard: The 1977 Gioia Tauro (Italy) landslide–tsunami investigated through numerical modeling. *Mar. Geol.* **357**, 210–217 (2014).
90. Fine, I. V., Rabinovich, A. B., Bornhold, B. D., Thomson, R. E. & Kulikov, E. A. The Grand Banks landslide-generated tsunami of November 18, 1929: preliminary analysis and numerical modeling. *Mar. Geol.* **215**, 45–57 (2005).
91. Molenaar, A., Moernaut, J., Wiemer, G., Dubois, N. & Strasser, M. Earthquake impact on active margins: tracing surficial remobilization and seismic strengthening in a slope sedimentary sequence. *Geophys. Res. Lett.* **46**, 6015–6023 (2019).
92. Sawyer, D. E., Reece, R. S., Gulick, S. P. S. & Lenz, B. L. Submarine landslide and tsunami hazards offshore southern Alaska: Seismic strengthening versus rapid sedimentation. *Geophys. Res. Lett.* **44**, 8435–8442 (2017).
93. Nelson, C. H., Escutia, C., Damuth, J. E. & Twichell, D. C. Interplay of mass-transport and turbidite-system deposits in different active tectonic and passive continental margin settings: external and local controlling factors. <https://pubs.geoscienceworld.org/sepm/books/edited-volume/1192/chapter/10715844> (2011). <https://doi.org/10.2110/SEPMSP.096.039>
94. Zhang, Z. et al. Landslide hazard cascades can trigger earthquakes. *Nat. Commun.* **15**, 2878 (2024).
95. Stucchi, M., Albin, P., Mirto, M. & Rebez, A. Assessing the completeness of Italian historical earthquake data. *Ann. Geophys.* **47**, <https://doi.org/10.4401/ag-3330> (2004).
96. Taroni, M. Estimating the magnitude of completeness of earthquake catalogs using a simple random variable transformation. *Seismic Rec.* **3**, 194–199 (2023).
97. Micallef, A., Georgiopoulou, A., Green, A. & Maselli, V. Impact of sea-level fluctuations on the sedimentation patterns of the SE African margin: implications for slope instability. *SP* **500**, 267–276 (2020).
98. Twichell, D. C., Chaytor, J. D., ten Brink, U. S. & Buczkowski, B. Morphology of late quaternary submarine landslides along the U.S. Atlantic continental margin. *Mar. Geol.* **264**, 4–15 (2009).
99. Piper, D. J. W., Cochonat, P. & Morrison, M. L. The sequence of events around the epicentre of the 1929 Grand Banks earthquake: initiation of debris flows and turbidity current inferred from sidescan sonar. *Sedimentology* **46**, 79–97 (1999).
100. Sulli, A., Lo Presti, V., Gasparo Morticelli, M. & Antonioli, F. Vertical movements in NE Sicily and its offshore: Outcome of tectonic uplift during the last 125 ky. *Quat. Int.* **288**, 168–182 (2013).
101. Tonini, R., Armigliato, A., Pagnoni, G., Zaniboni, F. & Tinti, S. Tsunami hazard for the city of Catania, eastern Sicily, Italy, assessed by means of worst-case credible tsunami scenario analysis (WCTSA). *Nat. Hazards Earth Syst. Sci.* **11**, 1217–1232 (2011).
102. Tinti, S. & Tonini, R. The UBO-TSUFDT tsunami inundation model: validation and application to a tsunami case study focused on the city of Catania, Italy. *Nat. Hazards Earth Syst. Sci.* **13**, 1795–1816 (2013).
103. Gutscher, M.-A., Roger, J., Baptista, M.-A., Miranda, J. M. & Tinti, S. Source of the 1693 Catania earthquake and tsunami (southern Italy): New evidence from tsunami modeling of a locked subduction fault plane. *Geophys. Res. Lett.* **33**, 2005GL025442 (2006).
104. Barbano, M. S., Pirrotta, C. & Gerardi, F. Large boulders along the south-eastern Ionian coast of Sicily: storm or tsunami deposits? *Mar. Geol.* **275**, 140–154 (2010).
105. Argnani, A. et al. Active tectonics along the submarine slope of south-eastern Sicily and the source of the 11 January 1693 earthquake and tsunami. *Nat. Hazards Earth Syst. Sci.* **12**, 1311–1319 (2012).
106. Mat Said, A., Ahmadun, F.-R., Rodzi Mahmud, A. & Abas, F. Community preparedness for tsunami disaster: a case study. *Disaster Prev. Manag. Int. J.* **20**, 266–280 (2011).
107. Lindell, M. K. & Prater, C. S. Tsunami preparedness on the Oregon and Washington coast: recommendations for research. *Nat. Hazards Rev.* **11**, 69–81 (2010).
108. Johnston, D. et al. Measuring tsunami preparedness in Coastal Washington, United States. *Nat. Hazards* **35**, 173–184 (2005).
109. Esteban, M. et al. Recent tsunamis events and preparedness: development of tsunami awareness in Indonesia, Chile and Japan. *Int. J. Disaster Risk Reduct.* **5**, 84–97 (2013).
110. Talling, P. J. et al. Longest sediment flows yet measured show how major rivers connect efficiently to deep sea. *Nat. Commun.* **13**, 4193 (2022).

111. Zaniboni, F., Armigliato, A. & Tinti, S. A numerical investigation of the 1783 landslide-induced catastrophic tsunamis in Scilla, Italy. *Nat. Hazards* **84**, 455–470 (2016).
112. Strasser, M., Jia, Y., Yamada, Y. & Urgeles, R. Introduction: Landslides in Coastal and Submarine Environments. in *Landslide Science for a Safer Geoenvironment* (eds Sassa, K., Canuti, P. & Yin, Y.) 545–548 (Springer International Publishing, 2014). https://doi.org/10.1007/978-3-319-04996-0_83.
113. Casas, D., Chiocci, F., Casalbore, D., Ercilla, G. & De Urbina, J. O. Magnitude–frequency distribution of submarine landslides in the Gioia Basin (southern Tyrrhenian Sea). *Geo-Mar. Lett.* **36**, 405–414 (2016).
114. Casalbore, D. et al. Morphological variability of submarine mass movements in the tectonically–controlled Calabro–Tyrrhenian Continental Margin (Southern Italy). *Geosciences* **9**, 43 (2019).
115. Blöthe, J. H., Korup, O. & Schwanghart, W. Large landslides lie low: Excess topography in the Himalaya–Karakoram ranges. *Geology* **43**, 523–526 (2015).
116. Li, G. K., Moon, S. & Higa, J. T. Residence Time of Over-Steepened Rock Masses in an Active Mountain Range. *Geophys. Res. Lett.* **49**, e2021GL097319 (2022).
117. Zei, C. et al. CFTI landslides, Italian database of historical earthquake-induced landslides. *Sci. Data* **11**, 834 (2024).
118. Sun, Q. et al. Slope deformation prior to Zhouqu, China landslide from InSAR time series analysis. *Remote Sens. Environ.* **156**, 45–57 (2015).
119. Dahal, A., Huser, R. & Lombardo, L. At the junction between deep learning and statistics of extremes: formalizing the landslide hazard definition. *J. Geophys. Res. Mach. Learn. Comput.* **1**, e2024JH000164 (2024).
120. Antonioli, F. et al. Sea-level rise and potential drowning of the Italian coastal plains: Flooding risk scenarios for 2100. *Quat. Sci. Rev.* **158**, 29–43 (2017).
121. Cazenave, A. et al. The rate of sea-level rise. *Nat. Clim. Change* **4**, 358–361 (2014).
122. Chiocci, F. L. et al. The Magic Project: large scale geohazard mapping of the Italian continental margins. in *Rendiconti online Società Geologica Italiana* vol. 7 17–19 (società geologica italiana, 2009).
123. Maltese, A., Presti, V. L., Nocera, G. A. & Sulli, A. Comparison of bathymetry estimated from multibeam echosounder and optical data. in *Remote Sensing for Agriculture, Ecosystems, and Hydrology XXVI* vol. 13191 26–32, <https://doi.org/10.1117/12.3038063> (SPIE, 2024).
124. Forfinski-Sarkozi, N. A. & Parrish, C. E. Active-passive spaceborne data fusion for mapping nearshore bathymetry. *Photogrammetric Eng. Remote Sens.* **85**, 281–295 (2019).
125. Leon, J. X., Phinn, S. R., Hamylton, S. & Saunders, M. I. Filling the ‘white ribbon’ – a multisource seamless digital elevation model for Lizard Island, northern Great Barrier Reef. *Int. J. Remote Sens.* **34**, 6337–6354 (2013).
126. D’Ascola, F., Cassese, M. L., Luger, N., Pesarino, V. & Salmeri, A. The ISPRA geodatabase for monitoring and analysis of the state of the Italian coasts: an example of its application to the Rocchette - Castiglione della Pescaia coast line. In *Ninth International Symposium “Monitoring of Mediterranean Coastal Areas: Problems and Measurement Techniques”* (eds Bonora, L., Carboni, D., De Vincenzi, M. & Matteucci, G.) (Firenze University Press, 2022). <https://doi.org/10.36253/979-12-215-0030-1.03>.
127. *MATLAB Version R2024a*. (The MathWorks, Inc., 2024).
128. European Space Agency & Airbus. Copernicus DEM. <https://doi.org/10.5270/ESA-c5d3d65> (ESA, 2022).
129. Schwanghart, W. & Scherler, D. Short communication: TopoToolbox 2 – MATLAB-based software for topographic analysis and modeling in Earth surface sciences. *Earth Surf. Dyn.* **2**, 1–7 (2014).
130. Geoportale RNDT. https://geodati.gov.it/resource/id/isprra_rm:01Idro250N_DT.
131. Wobus, C. et al. Tectonics from topography: Procedures, promise, and pitfalls. in *Tectonics, Climate, and Landscape Evolution* (eds Willett, S. D., Hovius, N., Brandon, M. T. & Fisher, D. M.) 0 (Geological Society of America, 2006). [https://doi.org/10.1130/2006.2398\(04\)](https://doi.org/10.1130/2006.2398(04)).
132. Palano, M., Piromallo, C. & Chiarabba, C. Surface imprint of toroidal flow at retreating slab edges: The first geodetic evidence in the Calabrian subduction system. *Geophys. Res. Lett.* **44**, 845–853 (2017).
133. Crosetto, M. et al. Deformation monitoring at European scale: the copernicus ground motion service. *Int. Arch. Photogramm., Remote Sens. Spat. Inf. Sci.* **XLIII-B3-2021**, 141–146 (2021).
134. Crosetto, M. et al. The evolution of wide-area DInSAR: from regional and national services to the European ground motion service. *Remote Sens.* **12**, 2043 (2020).
135. Ferranti, L. et al. Markers of the last interglacial sea-level high stand along the coast of Italy: Tectonic implications. *Quat. Int.* **145–146**, 30–54 (2006).
136. Casagli, N., Canuti, P., Sassa, K. & Tofani, V. The sixth world landslide forum (WLF6) on November 14–17, 2023, Florence, Italy. *Landslides* **19**, 2539–2545 (2022).
137. Burrato, P. et al. Mapping earthquake induced landslide hazard in Italy. in *Landslides* vol. 19 2539–2545 (Florence, 2023).
138. Boore, D. M. & Atkinson, G. M. Ground-motion prediction equations for the average horizontal component of PGA, PGV, and 5%-damped PSA at spectral periods between 0.01 s and 10.0 s. *Earthq. Spectra* **24**, 99–138 (2008).
139. Rovida, A., Locati, M., Camassi, R., Lolli, B. & Gasperini, P. *The Italian Earthquake Catalogue CPTI15. Bulletin of Earthquake Engineering* (Springer, 2020). <https://doi.org/10.1007/s10518-020-00818-y>.
140. Lorito, S., Tiberti, M. M., Basili, R., Piatanesi, A. & Valensise, G. Earthquake-generated tsunamis in the Mediterranean Sea: scenarios of potential threats to Southern Italy. *J. Geophys. Res.* **113**, 2007JB004943 (2008).
141. DISS Working Group. Database of Individual Seismogenic Sources (DISS), Version 3.3.0: A compilation of potential sources for earthquakes larger than M 5.5 in Italy and surrounding areas. <https://doi.org/10.13127/diss3.3.0> (2021).
142. Sakia, R. M. The box-cox transformation technique: a review. *J. R. Stat. Soc. Ser. D: Stat.* **41**, 169–178 (1992).
143. Henderi, H., Wahyuningsih, T. & Rahwanto, E. Comparison of min-max normalization and Z-Score normalization in the K-nearest neighbor (KNN) algorithm to test the accuracy of types of breast cancer. *Int. J. Inform. Inf. Syst.* **4**, 13–20 (2021).
144. Pham, H. A new criterion for model selection. *Mathematics* **7**, 1215 (2019).
145. Kokaly, R. F. & Clark, R. N. Spectroscopic determination of leaf biochemistry using band-depth analysis of absorption features and stepwise multiple linear regression. *Remote Sens. Environ.* **67**, 267–287 (1999).
146. Ghani, I. M. M. & Ahmad, S. Stepwise multiple regression method to forecast fish landing. *Procedia - Soc. Behav. Sci.* **8**, 549–554 (2010).
147. Powell, R. Regression diagnostics and robust regression in geothermometer/geobarometer calibration: the garnet-clinopyroxene geothermometer revisited. *J. Metamorphic Geol.* **3**, 231–243 (1985).
148. Fushiki, T. Estimation of prediction error by using K-fold cross-validation. *Stat. Comput.* **21**, 137–146 (2011).
149. O’Brien, R. M. A caution regarding rules of thumb for variance inflation factors. *Qual. Quant.* **41**, 673–690 (2007).
150. White, H. A heteroskedasticity-consistent covariance matrix estimator and a direct test for heteroskedasticity. *Econometrica: J. Econometric Soc.* 817–838 (1980). <https://doi.org/10.2307/1912934>
151. Halunga, A. G., Orme, C. D. & Yamagata, T. A heteroskedasticity robust Breusch–Pagan test for Contemporaneous correlation in dynamic panel data models. *J. Econ.* **198**, 209–230 (2017).

152. Razali, N. M. & Wah, Y. B. Power comparisons of Shapiro-Wilk, Kolmogorov-Smirnov, Lilliefors and Anderson-Darling tests. *J. Stat. Model. Anal.* **2**, 21–33 (2011).
153. Das, K. R. & Imon, A. A brief review of tests for normality. *Am. J. Theor. Appl. Stat.* **5**, 5–12 (2016).
154. Basi territoriali e variabili censuarie – Istat. <https://www.istat.it/notizia/basi-territoriali-e-variabili-censuarie/>.
155. Gnesko, L., Stahl, T., Mountjoy, J. J. & Carey, J. M. Transient evidence of shallow coseismic submarine landslides shaping canyon head geomorphology: insights from the 2016 Kaikōura earthquake, New Zealand. *Geology* (2025). <https://doi.org/10.1130/G53867.1>.
156. Pedrosa-González, M. T. et al. Simulation of tsunami induced by a submarine landslide in a glaciomarine margin: the case of Storfjorden LS-1 (southwestern Svalbard Islands). *Nat. Hazards Earth Syst. Sci.* **22**, 3839–3858 (2022).
157. Rashidi, A., Mokhtari, M., Goda, K., Masoodi, M. & Faridi, P. A landslide tsunami hazard assessment in the Makran Subduction Zone. *Mar. Geol.* **487**, 107580 (2025).
158. Nemati, F., Leonard, L., Thomson, R., Lintern, G. & Kouhi, S. Numerical modeling of a potential landslide-generated tsunami in the southern Strait of Georgia. *Nat. Hazards* **117**, 2029–2054 (2023).
159. Papadopoulos, G. A. & Kortekaas, S. Characteristics of Landslide Generated Tsunamis from Observational Data. In *Submarine Mass Movements and Their Consequences* (eds Locat, J., Mienert, J. & Boisvert, L.) vol. 19 367–374 (Springer, 2003). https://doi.org/10.1007/978-94-010-0093-2_40
160. Rodriguez, M. et al. Tsunamigenic submarine landslides along the Xauen–Tofiño banks in the Alboran Sea (Western Mediterranean Sea). *Geophys. J. Int.* **209**, 266–281 (2017).
161. Roger, J. H. M. et al. A review of approaches for submarine landslide-tsunami hazard identification and assessment. *Mar. Pet. Geol.* **162**, 106729 (2024).
162. Harbitz, C. B., Løvholt, F. & Bungum, H. Submarine landslide tsunamis: how extreme and how likely? *Nat. Hazards* **72**, 1341–1374 (2014).
163. Heidarzadeh, M., Gusman, A. R. & Mulia, I. E. The landslide source of the eastern Mediterranean tsunami on 6 February 2023 following the Mw 7.8 Kahramanmaraş (Türkiye) inland earthquake. *Geosci. Lett.* **10**, 50 (2023).
164. Rovida, A., Locati, M., Camassi, R., Lolli, B. & Gasperini, P. The Italian earthquake catalogue CPT115. *Bull. Earthq. Eng.* **18**, 2953–2984 (2020).
165. Ing. Cirone, S. & Ing. Scaffidi Abbate, P. Volo fotogrammetrico, LIDAR, ortofoto e cartografia. 1–59 (2009).
166. MacFerrin, M., Amante, C., Carignan, K., Love, M. & Lim, E. The Earth topography 2022 (etopo 2022) global dem dataset. *Earth Syst. Sci. Data Discuss.* **2024**, 1–24 (2024).
- 1243 2/8/2022, code PE0000005), and by the project ‘Space It Up!’ funded by the Italian Space Agency (ASI) and the Ministry of University and Research (MUR) (ASI Contract n. 2024-5-E.0, CUP I53D24000060005).

Author contributions

N.P. conceived the study, developed the methodology, performed the statistical analysis, prepared the figures, and wrote the original draft. F.C. assisted with data curation and dataset construction. P.B. contributed to the conceptualization and interpretation of the results. M.P. contributed to the conceptualization of the revisions and provided essential datasets. S.S., V.L.P., M.A., M.G.M., and A.S., together with the other authors, discussed the results, provided critical feedback, and contributed to the review and editing of the final manuscript.

Competing interests

The authors declare no competing interests.

Additional information

Supplementary information The online version contains supplementary material available at <https://doi.org/10.1038/s43247-026-03373-7>.

Correspondence and requests for materials should be addressed to Pierfrancesco Burrato.

Peer review information *Communications Earth and Environment* thanks Silvia Ceramicola, Morelia Urlaub and the other, anonymous, reviewer(s) for their contribution to the peer review of this work. Primary Handling Editors: Shan Liu, and Martina Grecequet. A peer review file is available.

Reprints and permissions information is available at <http://www.nature.com/reprints>

Publisher’s note Springer Nature remains neutral with regard to jurisdictional claims in published maps and institutional affiliations.

Open Access This article is licensed under a Creative Commons Attribution-NonCommercial-NoDerivatives 4.0 International License, which permits any non-commercial use, sharing, distribution and reproduction in any medium or format, as long as you give appropriate credit to the original author(s) and the source, provide a link to the Creative Commons licence, and indicate if you modified the licensed material. You do not have permission under this licence to share adapted material derived from this article or parts of it. The images or other third party material in this article are included in the article’s Creative Commons licence, unless indicated otherwise in a credit line to the material. If material is not included in the article’s Creative Commons licence and your intended use is not permitted by statutory regulation or exceeds the permitted use, you will need to obtain permission directly from the copyright holder. To view a copy of this licence, visit <http://creativecommons.org/licenses/by-nc-nd/4.0/>.

© The Author(s) 2026

Acknowledgements

This research received no specific grant from any funding agency in the public, commercial, or not-for-profit sectors. However, the work of some authors was supported by the project ‘RETURN Extended Partnership’ funded by the European Union Next-GenerationEU (National Recovery and Resilience Plan—NRRP, Mission 4, Component 2, Investment 1.3—D.D.